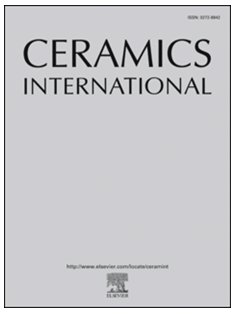

Development of a new carbon xerogel/ZnO/$BaSnO_3$ photocatalyst for solar and visible light photodegradation of salicylic acid

Flávio Henrique Covolam Boldrin, Laila Gazel de Andrade, Ikaro Tessaro, Bruno Henrique Baena da Silva, Robson da Silva Souto, Nicolas Perciani de Moraes, Robson da Silva Rocha, Marcos Roberto de Vasconcelos Lanza, Liana Alvares Rodrigues

PII: S0272-8842(24)04677-7

DOI: https://doi.org/10.1016/j.ceramint.2024.10.163

Reference: CERI 43461

To appear in: *Ceramics International*

Received Date: 2 July 2024

Revised Date: 10 October 2024

Accepted Date: 11 October 2024

Please cite this article as: F.H.C. Boldrin, L.G. de Andrade, I. Tessaro, B.H.B. da Silva, R.d. Silva Souto, N.P. de Moraes, R. da Silva Rocha, M.R.d.V. Lanza, L.A. Rodrigues, Development of a new carbon xerogel/ZnO/$BaSnO_3$ photocatalyst for solar and visible light photodegradation of salicylic acid, *Ceramics International*, https://doi.org/10.1016/j.ceramint.2024.10.163.

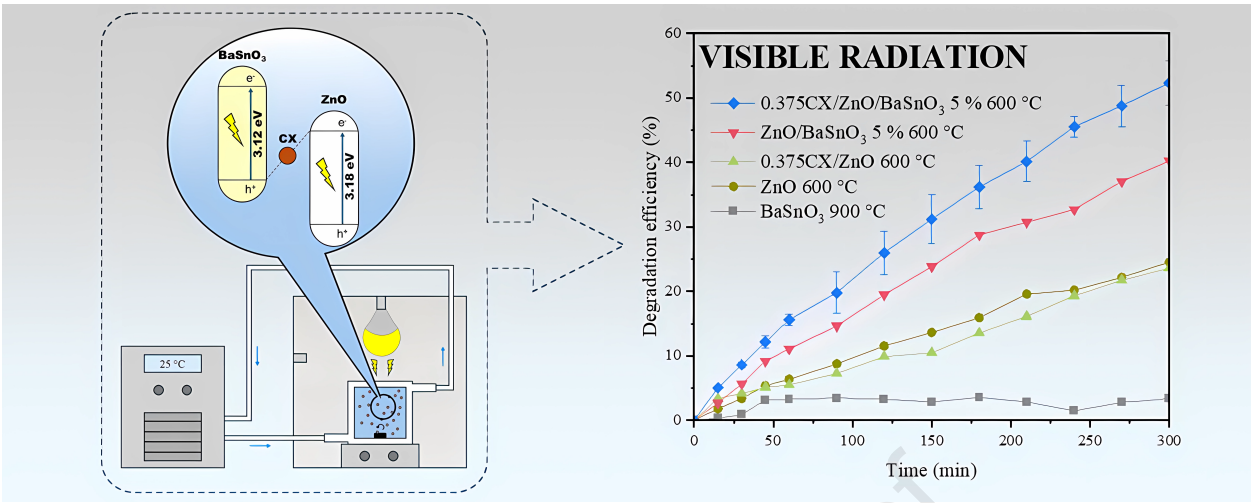

Development of a new carbon xerogel/ZnO/$BaSnO_3$ photocatalyst for solar and visible light photodegradation of salicylic acid

Flávio Henrique Covolam Boldrin[1], Laila Gazel de Andrade[1], Ikaro Tessaro[1], Bruno Henrique Baena da Silva[1], Robson da Silva Souto[2], Nicolas Perciani de Moraes[2], Robson da Silva Rocha[1], Marcos Roberto de Vasconcelos Lanza[2], Liana Alvares Rodrigues[1,*]

1- *Escola de Engenharia de Lorena-EEL/USP, Estrada Municipal do Campinho S/N, CEP 12602-810, Lorena, São Paulo, Brazil.*
2- *São Carlos Institute of Chemistry, University of São Paulo, Av. Trab. São Carlense, 400 - Parque Arnold Schimidt, São Carlos - SP, 13566-590*

Declarations of interest: none

*Corresponding author. Tel.: 55 1231595319; Fax: 55 1231595000

E-mail address: liana.r@usp.br

Abstract

A novel carbon xerogel/ZnO/$BaSnO_3$ photocatalyst was developed, characterized, and evaluated for the photodegradation of salicylic acid (SA) under solar and visible radiation. The development of the proposed photocatalyst involved the investigation of multiple synthesis parameters, aiming to optimize the photocatalytic activity of the ternary system. The best photocatalytic efficiency was obtained at 5 % w/w $BaSnO_3$, 0.375 g of added tannin, and calcination temperature of 600 °C, yielding the 0.375CX/ZnO/$BaSnO_3$ 5 % 600 °C photocatalyst. After thorough characterization, it was concluded that the ternary materials are composed of a mixture of crystalline ZnO and $BaSnO_3$ structures and carbon xerogel (CX). Additionally, the ternary materials displayed significant capacity to absorb visible radiation, mostly due to CX addition. Morphology-wise, the 0.375CX/ZnO/$BaSnO_3$ 5 % 600 °C was composed of nodular and polyhedral nanometric particles, displaying higher surface area when compared to materials without CX. Through chronoamperometry and electrochemical impedance spectroscopy, it was determined that the optimized ternary material achieved the highest photocurrent generation and lowest charge transfer resistance among the materials evaluated, indicating a superior photocatalytic activity. Photocatalytic tests demonstrated the superiority of the ternary system in the degradation of SA under solar and visible light irradiation, achieving 93 % and 52.3 % degradation after 5 h, respectively. The superior mineralization of SA (72.2 %) achieved by the optimized ternary material under solar radiation further demonstrated its increased efficacy. The suppression methodology allowed for the identification of the hydroxyl radical as the major active species in the SA degradation. A Z-type heterojunction was proposed for the ternary system, based on the staggered band alignment between ZnO and $BaSnO_3$ and the role of CX as a solid-state mediator, possibly leading to effective charge separation and enhanced redox activity. Phytotoxicity tests showed favorable *Lactuca sativa* growth in SA solutions treated with 0.375CX/ZnO/$BaSnO_3$ 5 % 600 °C (especially under solar radiation), indicating reduced toxicity.

Keywords: Carbon xerogel/ZnO/$BaSnO_3$, Heterogeneous photocatalysis, Salicylic acid, Z-type heterojunction

1. Introduction

The contamination of aquatic ecosystems by emerging pollutants (EPs) is an escalating environmental concern, primarily driven by the intensification of industrial activities and urban development [1]. This class of compounds, which includes pharmaceuticals and personal care products (PPCPs), industrial chemicals, and pesticides, has been increasingly detected in diverse water bodies globally. This accumulation is attributed to their recalcitrant nature and the limited removal efficiency of conventional water and wastewater treatment plants [1–5]. The subclass of PPCPs, which encompass drugs to prevent and treat human/animal diseases and products to improve human quality of life, presents a greater risk/toxicity to biota compared to other pollutants, such as pesticides and dyes, as their acquisition is mostly accessible to general population, which in turn renders supply control a difficult task. This factor, combined with their recalcitrant properties and indiscriminate discharge, makes their degradation/treatment a challenging endeavor [1–3,6].

Salicylic acid (SA), also known as 2-hydroxybenzoic acid, is classified as an EP among PPCPs and can be found in elevated concentration in natural water bodies, being one of the most commonly detected anti-inflammatory and analgesic drugs in groundwater (aquifers) [6,7]. Its occurrence can be linked to both the metabolization of acetylsalicylic acid and the disposal of cosmetics and food products. When consumed in large quantities, SA can cause a diverse range of symptoms, such as vomiting, abdominal pain, acidosis, and seizures [8,9]. Therefore, efficient degradation of salicylic acid is crucial to minimize its negative impacts on both the environment and human health.

In this context, heterogeneous photocatalysis emerges as a promising advanced oxidation technique, showing effectiveness in converting toxic pollutants into non-toxic compounds [10]. In this method, the absorption of irradiated photons by a semiconductor will lead to the excitation of electrons (e^-) from the valence band (VB) to the conduction band (CB), generating a hole (h^+) in the VB and an excess of electrons in the CB [8,11,12]. The presence of such electron-hole pairs in an aqueous system leads to the occurrence of redox chemical reactions and the subsequent generation of active radicals (such as OH• and $O_2^{\bullet-}$), which are able to drive the degradation of organic pollutants into non-toxic molecules, such as water and carbon dioxide [12,13].

Currently, titanium dioxide (TiO_2) is the most widely employed photocatalyst due to its low production cost, non-toxicity, and chemical stability; however, it experiences

rapid recombination of photogenerated charges due to strong Coulombic forces, along with a low specific surface area and limited absorption in the visible spectrum, hindering its efficacy in real-life applications [14–18]. ZnO has emerged as a potential substitute, offering similar characteristics in terms of cost, toxicity, and chemical stability [14–16]. Furthermore, ZnO presents some advantages: it absorbs a larger fraction of UV radiation (with a bandgap energy of 3.2 eV) and has better electron mobility, which implies reduced electrical resistance and more efficient electron transfer, leading to decreased electron/hole pair recombination [14,16,19,20]. However, the large bandgap of zinc oxide leads to limited absorption of visible light, making its application under natural light ineffective [14,19]. Additionally, ZnO is susceptible to photo corrosion under UV radiation and displays elevated recombination rates, although lower than those found for TiO_2 [21,22].

To address these limitations, a range of techniques can be implemented, including the structural modification of semiconductors, as well as the control of their morphology, surface defects, and interface properties through advanced engineering approaches. For instance, features such as semiconductor particle and crystallite sizes can impact the recombination rate of photogenerated charges (in nanoscale materials, for example, the reduced distance for photogenerated charge carriers to travel can lead to a decrease in recombination rates, thereby enhancing the efficiency of charge separation and transport) [23–25].

In this context, the formation of heterojunctions between semiconductors has shown promising results in overcoming many of the challenges associated with the low efficiency of single-component photocatalysts [26]. For instance, the use of perovskites for the formation of efficient heterojunctions has attracted significant interest from the scientific community, due to the possibility of more efficient charge transport, given their stable three-dimensional (AO_6) structure [27,28]. The use of barium stannate ($BaSnO_3$, with perovskite structure) emerges as a promising strategy to create efficient heterojunctions in conjunction with ZnO, aiming at the enhancement of its photocatalytic properties. In addition to its high photosensitivity, chemical stability, and low cost, $BaSnO_3$ has a suitable electronic structure for the creation of a staggered band alignment with ZnO and exhibits high charge mobility, contributing to photocatalytic efficiency of the proposed heterojunction [15,29–34]. Additionally, the addition of solid-state mediators, such as carbon xerogel (CX) produced from black acacia tannin, to the ZnO/$BaSnO_3$ system can bring additional benefits. Tannin-based carbon xerogel is a

reportedly low-cost material, derived from a renewable source, and possesses high stability, excellent electrical conductivity, and high specific surface area. These properties may lead to facilitated charge transfer and an increased interface available for the photocatalytic mechanism to occur. Additionally, the application of carbon-based materials as solid-state mediators has been reported to stabilize the Z-scheme heterojunction between semiconductors, favoring the redox potential of the system [14,35,36].

Therefore, this work aims to develop the CX/ZnO/$BaSnO_3$ hybrid photocatalyst as a promising strategy to increase the quantum efficiency of the photodegradation of EPs (with a focus on SA) through heterogeneous photocatalysis under visible and simulated solar radiation. The integration of the proposed materials may lead to the development of a more efficient, cost-effective, and environmentally sustainable photocatalytic system, facilitating the reduction of water body contamination and promoting the protection of both environmental ecosystems and human health.

2. Materials and methods

2.1. Synthesis

2.1.1. Synthesis of $BaSnO_3$

The methodology used for the preparation of $BaSnO_3$ was adapted from the one employed by Pandian and Sivakumar (2023), utilizing the coprecipitation method under ambient conditions followed by high-temperature calcination [37]. Initially, 2.38 g of $Ba(NO_3)_2$ (Vetec Química Fina Ltd.) was dissolved in 50 mL of deionized water (solution A). Similarly, 3.4 g of $SnCl_2.2H_2O$ (Dinâmica Química Ltd.) was added to 50 mL of deionized water (solution B). Both solutions were kept under magnetic stirring until complete dissolution of the salts was observed. Following the solubilization step, solution A was added to solution B, creating solution C. In another beaker, 3 g of NaOH (Synth) was dissolved in 50 mL of deionized water (solution D). After the complete dissolution of the NaOH, solution D was added to solution C under constant stirring to precipitate the material. This solution was then transferred to a closed container and left without agitation for 24 h, after which the resulting precipitate was filtered, washed with deionized water until neutral pH, dried in an oven at 80 °C until constant mass, ground and sieved using a 325-mesh sieve (45 mm). Finally, the white-colored powder obtained was calcined at the temperature of 900 °C for 3 h in a tubular furnace to acquire the desired material ($BaSnO_3$).

2.1.2. Synthesis of ZnO

Firstly, 17.76 g of $Zn(NO_3)_2.6H_2O$ (Synth) was dissolved in 50 mL of deionized water (solution A) and 7.26 g of KOH was dissolved in 50 mL of deionized water (solution B). After dissolution, solution B was added to solution A. Subsequently to the precipitation, the obtained material was washed until neutral pH, dried in an oven at 80 °C until a constant mass was observed, ground, and sieved through a 325 mesh sieve (45 mm). The calcination process was carried out at 600 °C for 30 min under a N_2 atmosphere in a muffle furnace.

2.1.3. Synthesis of CX/ZnO/$BaSnO_3$, CX/ZnO and ZnO/$BaSnO_3$ composites

The synthesis methodology of the ternary materials was adapted from the one proposed by Moraes et al. (2024), where tannin was used in the presence of ZnO for the formation of the carbon xerogel [38]. Initially, 17.76 g of $Zn(NO_3)_2.6H_2O$ (Synth) were dissolved in 30 mL of deionized water (solution A) and a known amount of tannin (Phenotan AP provided by Tanac S.A.) was dissolved in 20 mL of deionized water (solution B). After dissolution, solution B was added to solution A, forming solution C. Subsequently, a known amount of previously synthesized $BaSnO_3$ was dispersed in solution C under the action of an ultrasonic bath (CRISTÓFOLI 50/60 Hz). After complete dispersion of $BaSnO_3$ in solution C, a previously prepared solution D with 7.26 g of KOH (Neon) and 50 mL of deionized water was added, still under the action of the ultrasonic bath, for the precipitation of the ternary material. The precipitate was then washed with deionized water until reaching neutral pH, dried in an oven at 80 °C until constant mass, ground, and sieved through a 325 mesh sieve (45 mm). The resulting materials were calcined at known temperatures for 30 min in a muffle furnace with a heating rate of 10 °C min^{-1} under N_2 atmosphere. The steps involved in the synthesis process can be better understood in the scheme proposed in *Figure 1*.

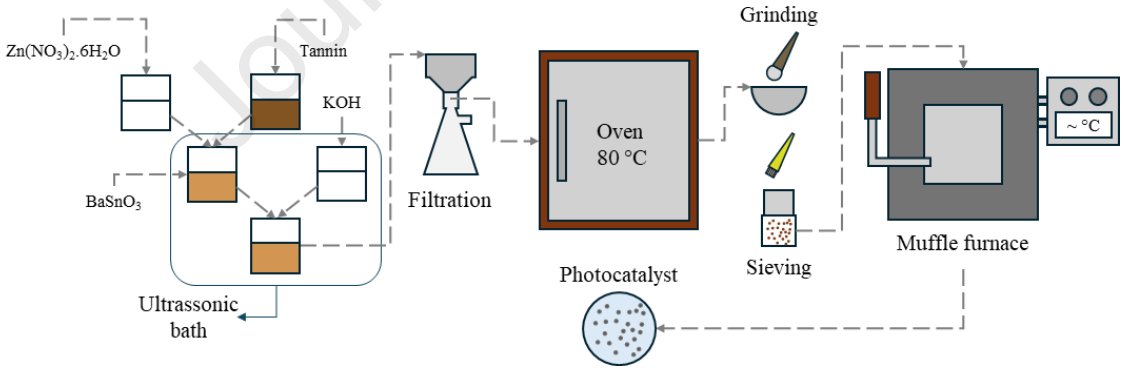

Fig. 1 - Synthesis procedure used for the production of photocatalysts based on CX/ZnO/$BaSnO_3$

The optimization of the CX/ZnO/$BaSnO_3$ hybrid photocatalyst was performed through the modification of various synthesis parameters. All syntheses adhered to the same methodology described previously, where the parameters were evaluated in the following sequence: variations in the amounts of $BaSnO_3$ used, variations in the tannin content employed, and variations in the calcination temperature. The specific parameters for each synthesis are detailed in *Table 1*. The materials described here adhere to the

following notation: m_gCX/ZnO/$BaSnO_3$ t % T ºC, where: m_g represents the mass of tannin added for the formation of CX/ZnO/$BaSnO_3$, t % denotes the mass percentage of $BaSnO_3$ relative to ZnO, and T ºC indicates the calcination temperature in degrees Celsius.

Tab. 1 - Specified parameters for all the ternary materials synthesized.

Materials	$BaSnO_3$ (g) added	Tannin (g) added	Calcination (°C)
0.375CX/ZnO/$BaSnO_3$ 1 % 600 °C	0.049	0.375	600
0.375CX/ZnO/$BaSnO_3$ 2.5 % 600 °C	0.124	0.375	600
0.375CX/ZnO/$BaSnO_3$ 5 % 600 °C	0.255	0.375	600
0.375CX/ZnO/$BaSnO_3$ 7.5 % 600 °C	0.392	0.375	600
0.375CX/ZnO/$BaSnO_3$ 10 % 600 °C	0.537	0.375	600
0.250CX/ZnO/$BaSnO_3$ 5 % 600 °C	0.255	0.250	600
0.500CX/ZnO/$BaSnO_3$ 5 % 600 °C	0.255	0.500	600
0.375CX/ZnO/$BaSnO_3$ 5 % 300 °C	0.255	0.375	300
0.375CX/ZnO/$BaSnO_3$ 5 % 400 °C	0.255	0.375	400
0.375CX/ZnO/$BaSnO_3$ 5 % 500 °C	0.255	0.375	500
0.375CX/ZnO/$BaSnO_3$ 5 % 700 °C	0.255	0.375	700

The syntheses of the binary composites followed the same methodology described for the ternary materials, and the parameters used for their syntheses were the same as those employed for the ternary 0.375CX/ZnO/$BaSnO_3$ 5 % 600 °C. However, in the case of 0.375CX/ZnO 600 °C, no $BaSnO_3$ was added, and for ZnO/$BaSnO_3$ 5 % 600 °C, no tannin was added.

2.2. Characterization

X-ray diffraction measurements were used to identify the crystalline phases present in the materials. The analyses were conducted using a PANalytical Empyrean X-ray equipment operating at 40 kV and 30 mA with a copper tube (CuKα radiation, λ=0.15418 nm). Scans were performed with a step size of 0.013 ° in 2θ and an acquisition time of 0.06 seconds per step, covering the 2θ range from 20 to 70 °.

Scanning electron microscopy (SEM) was utilized to observe the morphology of the materials. A TESCAN MIRA 3 scanning electron microscope with a field emission gun was employed for this purpose. The elemental composition of the best ternary photocatalyst and its corresponding binary and unary materials was determined using energy-dispersive spectroscopy (EDS), performed with an Oxford Swift ED3000 spectrometer coupled to the SEM. Furthermore, for transmission electron microcopy (TEM) a JEOL JEM-2100 LaB6 microscope, operated at 200 kV and equipped with a Gatan 2 K digital camera, was employed.

N_2 adsorption-desorption isotherms were measured at -196 °C using a V-Sorb 2800 adsorption analyzer. Prior to analysis, the materials were degassed under vacuum at 120 °C. BET (Brunauer Emmett Teller) method was employed to determine the specific surface areas, while the total pore volume of the samples was estimated using the relative pressure of P/P_0~0.99.

The chemical structure of the materials was characterized by Fourier-transform infrared spectroscopy (FTIR), using a universal attenuated total reflectance (UATR) accessory on a Perkin Elmer Frontier spectrometer. Analyses were performed in the range of 4000 to 500 cm^{-1} with a resolution of 4 cm^{-1}, involving 16 scans for each analysis. Raman spectroscopy was also conducted for the evaluation of the chemical structure of the materials, employing a LabRAM HR Evolution Raman Spectrometer equipped with an argon ion laser. Spectra were recorded within the range of 100 to 1800 cm^{-1}, with a 60-second acquisition time for each cycle.

Diffuse reflectance spectroscopy (DR) was conducted to determine the bandgap energy of the samples, absorption range, and energy levels of the conduction and valence bands. A Shimadzu UV-2600 spectrophotometer equipped with an ISR2600 Plus integrating sphere was used for this purpose, with barium sulfate as the standard.

Chronoamperometry and electrochemical impedance spectroscopy tests were performed to study the photocurrent generation and the charge transfer resistance of the best ternary material and its corresponding binary and unary counterparts. A Metrohm Autolab potentiostat was used for these tests. The photocurrent generation and electrochemical impedance for each material were determined using the porous microlayer technique, under simulated solar radiation. A thin layer of each material was deposited on an RDE electrode (Pine Research, model AFE3T050PTPK), with a platinum foil used as the counter electrode and an Ag/AgCl reference electrode. The electrolyte used was a potassium sulfate solution (0.1 mol L^{-1}) placed in a 200 mL quartz cell. For

the chronoamperometry, the tests were performed for each material by applying a potential of 0.8 V (vs AgCl) for 700 s, with light irradiation periods of 60 s. For the EIS, the tests were performed by applying the same potential of 0.8 V in a frequency range of 1000 to 0.01 Hz with an amplitude of 0.1 V_{rms}.

2.3. Photocatalytic evaluation

The methodology for the photocatalytic evaluation followed the approach adopted by Moraes et al. (2021) [39]. The tests were performed in a 0.5 L jacketed batch reactor with constant magnetic stirring and a reaction temperature of 25 °C, maintained with the aid of a thermostatic bath. In each test, 0.1 g of the evaluated photocatalyst and 0.5 L of pollutant solution (SA, 10 mg L^{-1}) were added to the reactor, and the reaction system was kept in the dark until adsorption-desorption equilibrium was reached. Subsequently, the samples were exposed to irradiation from an artificial light source using an Osram Ultra-vitalux 300 W lamp for simulated solar radiation and an Osram Powerstar HQI-T 400 W lamp for visible radiation. The concentration of SA was analyzed using a UV-visible spectrophotometer at a characteristic wavelength (296 nm for SA), and all the samples were filtered using disposable 0.22 µm nylon filters. The setup used for the conducted tests can be observed in *Figure 2*.

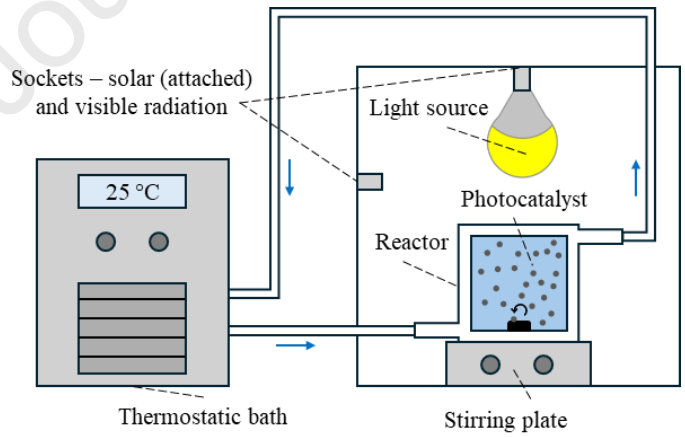

Fig. 2 – System assembled to perform the photocatalytic tests

To assess both the adsorption-desorption equilibrium and the initial hour of degradation, a sampling interval of 15 min was established, followed by subsequent aliquots taken at 30-minute intervals. The photocatalytic experiments were performed for

5 h (following the adsorption-desorption equilibrium process). Subsequently, the degradation efficiency was assessed using *Equation 1*.

$$Degradation\ efficiency\ (\%) = \frac{C_0 - C}{C_0} * 100 \qquad eq.1$$

Where: C_0 represents the pollutant concentration after the adsorption-desorption equilibrium; C represents the concentration at a given time (*t*).

To validate the measurements obtained by UV spectroscopy, the concentration of SA (for tests using both solar and visible radiation) was also assessed through high-performance liquid chromatography (HPLC) for the best ternary photocatalyst. The tests were conducted in the same manner as mentioned above, with aliquots filtered through disposable 0.22 µm nylon filters and stored in 2 mL vials. Samples were taken at the same time intervals described previously. A Shimadzu HPLC model LC-20 AT was employed for the measurements, equipped with a Phenomenex Luna C-18 column and a mobile phase consisting of 30 % water and 70 % acetonitrile. The flow rate was maintained at 1 mL min^{-1}, with an injection volume of 50 µL. A UV detector set to a wavelength of 200 nm was used to conduct the measurements.

Additionally, for the optimized ternary material, as well as its corresponding binary and unary forms, tests were conducted to assess their capacity to mineralize the target pollutant, salicylic acid (SA). These tests followed the same procedure as the degradation experiments, with aliquots of approximately 10 mL collected at the beginning (0 min), mid-point (180 min), and conclusion of the experiment (300 min). A total organic carbon analyzer (TOC-V CPN, Shimadzu) was employed for this evaluation, using the non-purgeable organic carbon (NPOC) method to determine the total purgeable organic carbon content in the collected aliquots.

The mechanism of active radical generation using the optimized ternary material was evaluated through tests with suppression agents for each active radical, as described below: electron-hole – sodium oxalate (0.5 mmol L^{-1}); electron – potassium chromate (0.05 mmol L^{-1}); superoxide – nitrogen (0.3 L min^{-1}); hydroxyl – isopropanol (4 % v/v) [22]. The tests were carried out over 180 min under solar radiation with the same parameters described previously.

Phytotoxicity bioassays were conducted to confirm the reduction of toxicity in pollutant-containing solutions following treatment with the optimal ternary photocatalyst

under both solar and visible light irradiation. The study using plant bioindicators stands out as a reliable and cost-effective approach for ecotoxicological assessments, offering sensitivity in detecting adverse effects, low cost, and ease of implementation. Evaluating the allelopathic activity in treated effluents is crucial for understanding the direct effects of the presence of xenobiotics in the environment [40,41]. Lettuce seeds (*Lactuca sativa*) were selected for this study due to their high sensitivity, ease of acquisition, independence from seasonal variations, and capacity to provide extensive quantitative data, including measurements of root growth and shoot development in germinated seedlings [42,43].

The experiments were carried out using 90 mm diameter Petri dishes (cleaned and dried at 100 ºC for 15 min) with filter paper of matching diameter. The study assessed the effects of four solutions on root elongation, shoot development, and overall seedling length. These solutions comprised a standard concentration of 10 mg L^{-1} of SA, a post-treatment solution using the most effective ternary photocatalyst under solar radiation, another post-treatment solution using the same photocatalyst under visible radiation (both treated solutions were obtained following the aforementioned methodology, undergoing batch reactor treatment for 5 h using different radiation sources), and a control solution of deionized water. Following a 4-day incubation period at 30 ºC with a 12-hour photoperiod in an oven, measurements were taken for root length, shoot length, and total seedling length. All tests were performed in triplicate, with each replicate consisting of a set of 5 seeds or germinated seedlings and, subsequently, the results underwent analysis of variance, and mean comparisons were conducted utilizing Tukey's test with a 95 % confidence level [44].

Finally, reaction parameters (SA concentration, photocatalyst dosage, salinity, and pH) were varied to assess the photocatalytic efficiency of the best ternary composition under different reaction conditions. The pH of the SA solution was adjusted using HCl (0.1 mol L^{-1} - LS Chemicals) and NaOH (0.1 mol L^{-1} - Synth), and the salinity was altered with NaCl [45]. All tests were conducted under solar radiation following the same procedure described for the degradation assays.

3. Results and discussion

3.1. Characterization

Figure 3 shows the diffractograms obtained for the unary materials ZnO 600 °C and $BaSnO_3$ 900 °C.

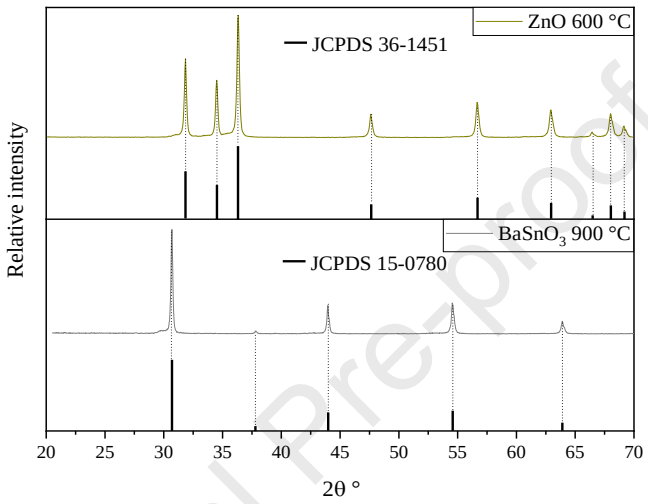

Fig. 3 - Comparison of X-ray diffraction patterns of unary materials (ZnO 600 °C and $BaSnO_3$ 900 °C) with their respective JCPDS cards

According to *Figure 3*, the characteristic peaks of the cubic crystal structure (perovskite) of $BaSnO_3$ were observed at the positions 30.7 °, 37.8 °, 44.0 °, 54.6 °, and 63.9 °, which align with the values found in the JCPDS card 15-0780, representing the (110), (111), (200), (211), (220) reflection planes, respectively [46]. For the zinc oxide (ZnO), the characteristic peaks of the hexagonal crystal structure (wurtzite) were observed at the positions 31.8 °, 34.4 °, 36.3 °, 47.5 °, 56.6 °, 62.8 °, 66.3 °, 67.9 °, and 69.1 °, which agree to the angular values specified in the JCPDS card 36-1451, representing the (100), (002), (101), (102), (110), (103), (200), (112), and (201) reflection planes, respectively [47].

Figure 4 illustrates the comparison of the diffractograms for the ternary CX/ZnO/$BaSnO_3$ materials with variations in synthesis parameters (as detailed in *Table 1*), alongside those of the binary and unary materials.

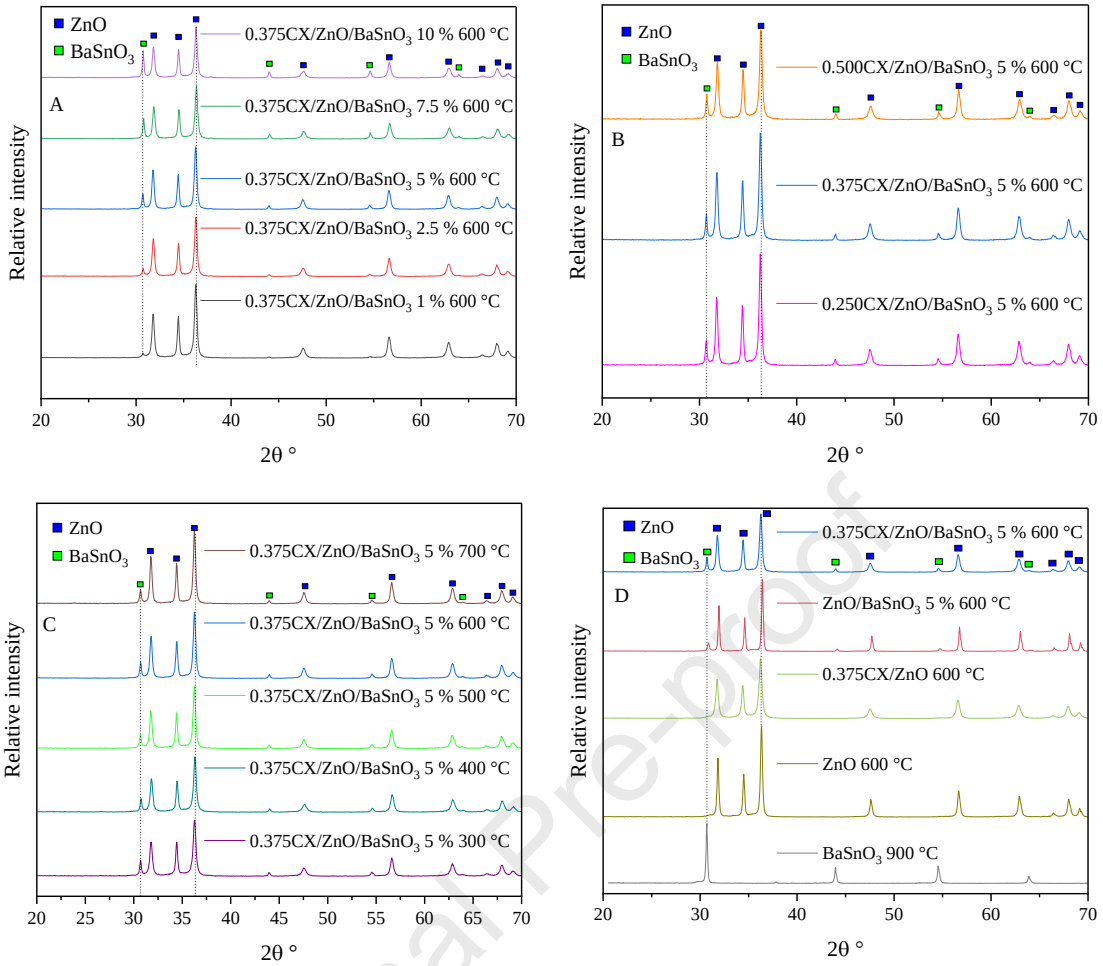

Fig. 4 - X-ray diffraction (XRD) patterns obtained for the materials synthesized in this study: A) Ternaries with different quantities of $BaSnO_3$ (1-10 %); B) Ternaries with different quantities of added tannin (0.25-0.50 g); C) Ternaries with different calcination temperatures (300-700 °C); D) Comparison between the ternary composite and its binary and unary counterparts

Similarly to the unary materials previously described, all ternary and binary composites displayed characteristic peaks corresponding to their constituent compounds, with peaks located at representative positions of the crystalline structures of ZnO (wurtzite) and $BaSnO_3$ (perovskite) for the ternaries and binary ZnO/$BaSnO_3$ 5 % 600 °C, and peaks only referring to ZnO in the case of the binary 0.375CX/ZnO 600 °C [46,47]. In all ternaries, a slight shift in the position of the ZnO peaks (*Figures 4A, B, C, D*) can be noticed at lower angles, which may indicate the addition of carbon into the ZnO crystal lattice [48]. Additionally, regarding the variation in the content of $BaSnO_3$ (*Figure 4A*), as its content increased in the ternary materials, a trend towards a decrease in the intensity of the ZnO peaks was identified, probably due to the lower amount of ZnO in the composites [48,49].

However, upon comparing the peak positions of ZnO/$BaSnO_3$ 5 % 600 °C with the unary ZnO 600 °C (*Figure 4D*), a variation in the peak positions of ZnO in the binary towards higher angles was observed, indicating that the distortion of the ZnO crystal structure by $BaSnO_3$ had an opposite effect to carbon, as similarly observed for other ZnO-based materials in the literature, such as those composed of ZnO/g-C_3N_4 and ZnO/ZnS [48,50].

The Scherrer equation (*Equation 2*) was used to calculate the crystallite size of all materials, as shown in *Table 2* [48,51,52].

$$L_c = \frac{0.9 \times \lambda}{\beta_c \times \cos(\theta)} \qquad eq.2$$

Where: L_c is the size of the crystallite in nm; λ is the wavelength generated from the tube used in the equipment, in this case, copper radiation ($\lambda_{CuK\alpha} = 0.154\,nm$); θ represents the diffraction angle of the peak with the greatest intensity; β_c is the width at half-height of the peak with the greatest intensity [48,51,52].

Tab. 2 - Crystallite sizes of all materials produced in this study

Material	**L_c (nm)**	**Material**	**L_c (nm)**
$BaSnO_3$ 900 °C	46.264	0.375CX/ZnO/$BaSnO_3$ 10 % 600 °C	30.057
ZnO 600 °C	34.971	0.250CX/ZnO/$BaSnO_3$ 5 % 600 °C	28.616
0.375CX/ZnO 600 °C	25.091	0.500CX/ZnO/$BaSnO_3$ 5 % 600 °C	25.040
ZnO/$BaSnO_3$ 5 % 600 °C	43.544	0.375CX/ZnO/$BaSnO_3$ 5 % 300 °C	25.403
0.375CX/ZnO/$BaSnO_3$ 1 % 600 °C	25.953	0.375CX/ZnO/$BaSnO_3$ 5 % 400 °C	26.363
0.375CX/ZnO/$BaSnO_3$ 2.5 % 600 °C	26.530	0.375CX/ZnO/$BaSnO_3$ 5 % 500 °C	26.359
0.375CX/ZnO/$BaSnO_3$ 5 % 600 °C	28.040	0.375CX/ZnO/$BaSnO_3$ 5 % 700 °C	30.057
0.375CX/ZnO/$BaSnO_3$ 7.5 % 600 °C	27.314		

From *Table 2*, it was observed that the materials with larger crystallite sizes are $BaSnO_3$ and the binary ZnO/$BaSnO_3$ 5 % 600 °C, followed by ZnO. On the other hand, a reduction in crystallite size was observed in all ternary materials, as well as in the binary 0.375CX/ZnO 600 °C. Additionally, it was observed that the increase in the amount of

added tannin, the content of $BaSnO_3$, and the calcination temperature had inversely, directly, and directly proportional effects on the increase in crystallite size, respectively.

The reduction in crystallite size with increasing amounts of tannin added during the synthesis of the ternaries demonstrates the influence of carbon xerogel addition to the structure, as the tannin molecules in the system act as nucleating agents for zinc oxide particles; thus, the smaller crystallite sizes are attributed to the greater availability of nucleation sites [14,48]. The observed increase in crystallite size with higher amounts of $BaSnO_3$ and higher calcination temperatures in the ternaries can be explained as follows: intuitively, this increase is attributed to the larger crystallite size of the pure $BaSnO_3$, whereas the higher calcination temperatures facilitate the coalescence of smaller crystallites into larger ones [53].

Considering that crystallite size is inversely correlated with photocatalytic activity, where smaller crystallites are reportedly linked to enhanced photocatalytic performances, it can be inferred that the addition of tannin to the ternary system may positively impact its photocatalytic efficiency [54,55]. Furthermore, the influence of synthesis parameters on crystallite size highlights the critical role of optimizing these variables in the context of photocatalyst development, with the goal of creating a more efficient system.

Figure 5 shows the comparison of the FTIR spectrum of the ternary materials CX/ZnO/$BaSnO_3$ with variations in synthesis parameters, as shown in *Table 1*, as well as those of the binary and unary materials.

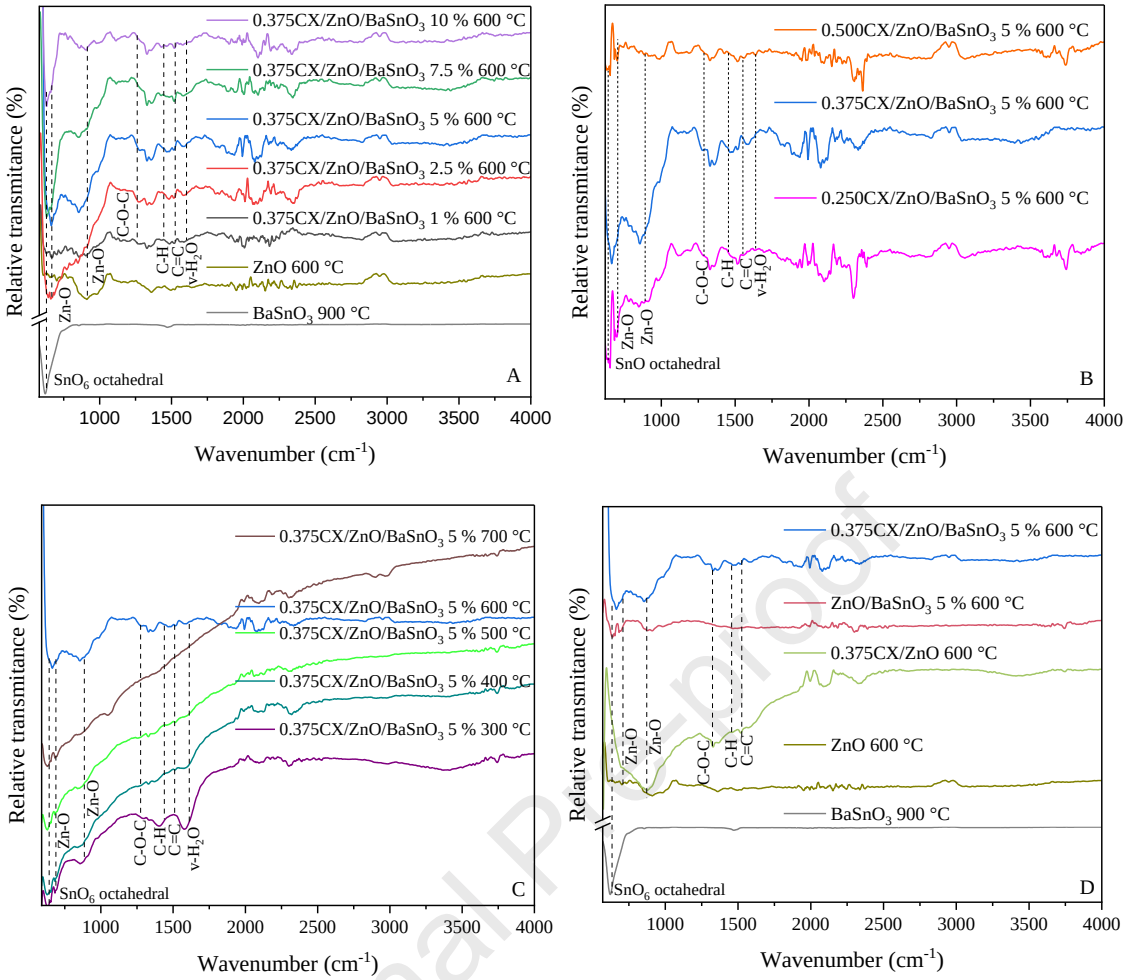

Fig. 5 – FTIR spectra obtained for the materials synthesized in this study: A) Ternaries with different quantities of $BaSnO_3$ (1-10 %); B) Ternaries with different quantities of added tannin (0.25-0.50 g); C) Ternaries with different calcination temperatures (300-700 °C); D) Comparison between the ternary composite and its binary and unary counterparts

According to *Figures 5A, B, C, and D*, representative peaks of the bonds present in each individual component of the materials could be observed. All materials containing $BaSnO_3$ (m_gCX/ZnO/$BaSnO_3$ t % T ºC, ZnO/$BaSnO_3$ 5 % 600 °C, and $BaSnO_3$ 900 °C) showed a peak at 645 cm^{-1}, related to stretching vibrations of the {SnO_6} octahedral, typical of $BaSnO_3$. Additionally, a peak at 1476 cm^{-1} was identified in the unary $BaSnO_3$, which may be related to the stretching vibration of Sn-OH, possibly due to moisture absorption by the material [56–59]. The peaks at 720 and 905 cm^{-1}, which appeared in all ternary, binary, and unary ZnO samples, are related to the Zn-O bonds. Additionally, the peaks at 1260, 1440, and 1520 cm^{-1} found in all ternary samples and binary 0.375CX/ZnO 600 °C are related, respectively, to the existence of C-O-C bonds (formed during the polycondensation of the tannin-based carbon xerogel), stretching vibrations of CH_2

groups, and C=C bonds (present in trisubstituted benzene rings), all of which can be linked with the presence of carbon xerogel in the materials [54,60,61].

Furthermore, a peak at 1600 cm^{-1} and a larger peak between 3000 and 3500 cm^{-1} were observed (mainly in the materials with lower calcination temperatures), indicating, respectively, the presence of adsorbed water and hydrogen bonds; these hydrogen bonds can be related to carboxyl and phenolic groups, as well as adsorbed water. Finally, the tendency towards an increase in intensity observed for the peak at 645 cm^{-1} in *Figure 5A* is consistent with the increase in the $BaSnO_3$ content in the syntheses of these materials [54,56].

In addition, to gain a deeper understanding of the composition of the 0.375CX/ZnO/$BaSnO_3$ 5 % 600 °C ternary material in comparison with the binary systems (ZnO/$BaSnO_3$ 5 % 600 °C and 0.375CX/ZnO 600 °C) and the unary materials (ZnO 600 °C and $BaSnO_3$ 900 °C), Raman spectroscopy was conducted. The results are presented in *Figure 6*.

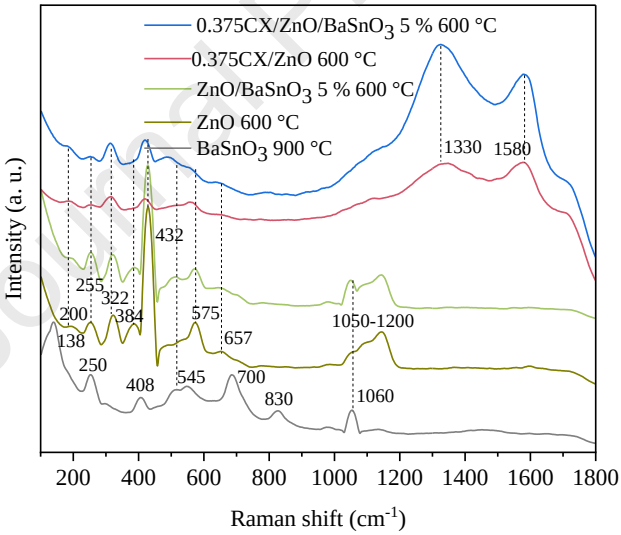

Fig. 6 - Raman spectrum of the 0.375CX/ZnO/$BaSnO_3$ 5 % 600 °C material in comparison with ZnO/$BaSnO_3$ 5 % 600 °C, 0.375CX/ZnO 600 °C, ZnO 600 °C, and $BaSnO_3$ 900 °C

The perovskite structure of barium stannate reportedly does not exhibit first-order Raman peaks due to its centrosymmetric crystalline structure, so the observed peaks can possibly be attributed to defects created by its high calcination temperature. Based on *Figure 6*, in the case of $BaSnO_3$, the presence of peaks at 138, 408, 545, 700, 830, and 1060 cm^{-1} was identified, corresponding to the vibrational modes of the SnO_6 octahedron in the perovskite structure, which has O_h symmetry. More specifically, the Raman active

modes v_2E_g, and v_5F_{2g} were observed at the peaks of 545 and 138 cm^{-1}, respectively, and the peak at 250 cm^{-1} may be associated with the (TO_2) optical phonon mode [56,62,63]. As for ZnO, peaks were observed at 200, 255, 322, 384, 432, 575, and 657 cm^{-1}, along with a broad band between 1050 and 1200 cm^{-1}, which can be associated with characteristic ZnO peaks reported in the literature, corresponding to the following modes: $2E_2$ (low) mode, B_1 (low) silent mode, E_2 (high) – E_2 (low) mode, A_1 (TO) mode, E_2 (high) mode, A_1 (LO) mode, E_1 E_2 (LA+TO) mode, and acoustic combination of A_1 and E_2 modes, respectively [48,64,65].

According to the dashed lines in *Figure 6*, it is evident that most of the peaks observed for ZnO were also detected in the hybrids containing this material, indicating its incorporation into the composites. Furthermore, given the low amount of $BaSnO_3$ in the composite materials evaluated and the significant overlap of peaks between ZnO and $BaSnO_3$, only the peaks at 545 and 1060 cm^{-1} could be identified in the ternary material and binary ZnO/$BaSnO_3$ 5 % 600 °C, which nonetheless supports the $BaSnO_3$ presence in the hybrid materials. Lastly, the bands at 1330 and 1580 cm^{-1} observed in the materials containing carbon xerogel can be attributed to the D and G bands of carbon, respectively [48,64].

Figure 7 presents the absorption spectra obtained by diffuse reflectance for all the materials synthesized in this work.

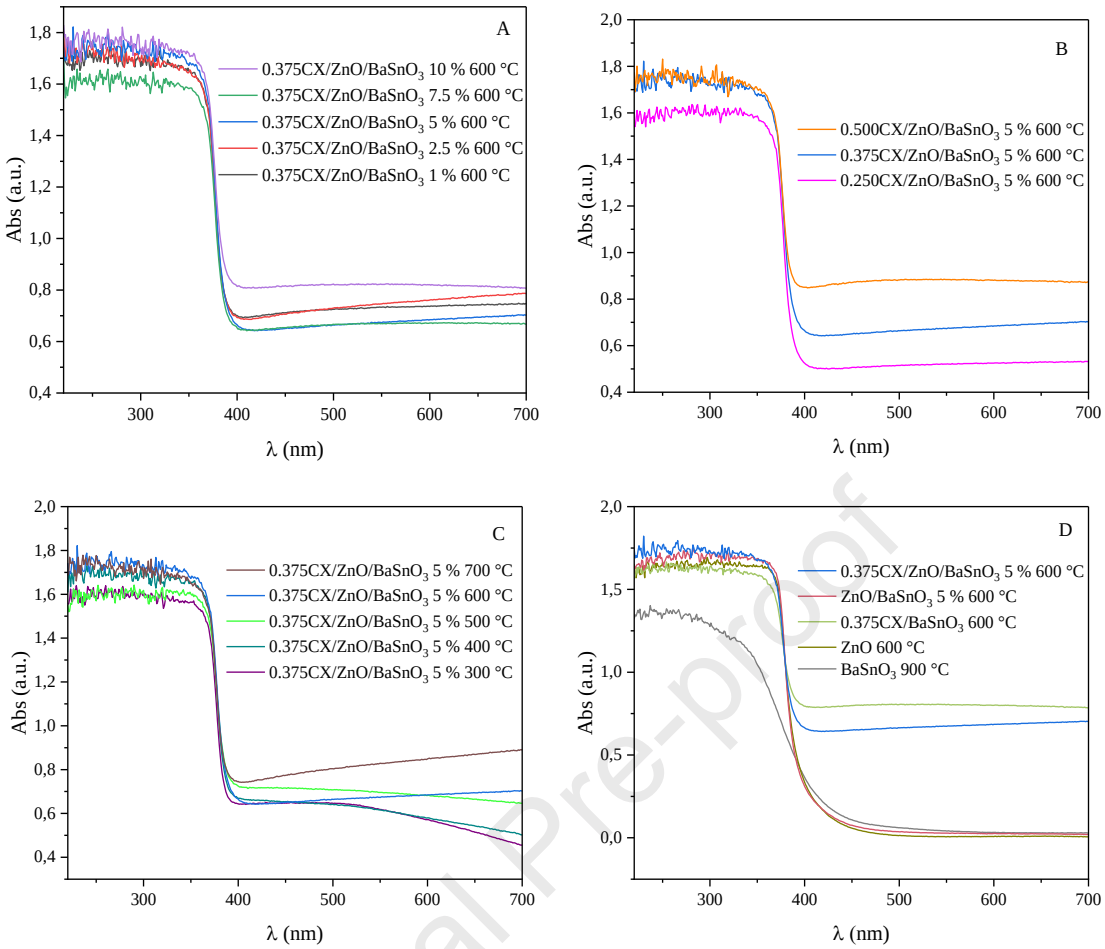

Fig. 7 – Diffusive reflectance spectra obtained for the materials synthesized in this study: A) ternaries with different quantities of $BaSnO_3$ (1-10 %); B) ternaries with different quantities of added tannin (0.25-0.50 g); C) ternaries with different calcination temperatures (300-700 °C); D) comparison between the ternary composite and its binary and unary counterparts

Figure 7D shows that the unary materials ZnO 600 °C and $BaSnO_3$ 900 °C have low absorption capacity at wavelengths higher than 500 nm, with $BaSnO_3$ exhibiting slightly superior absorption capacity at higher wavelengths compared to ZnO, congruent with results found in the literature [16,66,67]. However, the unexpected absorption capacity of ZnO for wavelengths higher than 420 nm can be explained by the probable presence of oxygen vacancies, leading to the creation of an isolated defect state below the ZnO conduction band, indicating possible activity under visible radiation [22]. Additionally, the binary ZnO/$BaSnO_3$ 5 % 600 °C presented results comparable to ZnO, but with a small increase in absorbance in higher wavelengths, similar to what was observed for $BaSnO_3$, possibly indicating the influence of its addition to the system, leading to better photocatalytic results under visible radiation.

After analysis of *Figures 7A, B, C, and D*, it was found that all materials containing carbon xerogel exhibited improved absorption capabilities at longer

wavelengths, confirming that the addition of carbon to the structure enhances sensitivity in the visible spectrum [22,61]. Both the variation in tannin and the variation in calcination temperature showed an influence on the absorbance of the materials at longer wavelengths in a directly proportional manner. That is, as the amount of tannin added and the calcination temperature increased, the absorbance of the materials in the visible spectrum region also increased. These phenomena highlight the synergy between the carbonaceous matrix and the oxides in the ternary compounds, as well as favorable results for calcination at higher temperatures regarding photoexcitation in the visible region [14,39].

Through diffuse reflectance spectroscopy analysis, it was also possible to obtain the bandgaps corresponding to each of the tested materials. For this purpose, a methodology proposed by [68] was employed, using the Tauc relation (*Equation 3*).

$$\left(\frac{Abs}{\lambda}\right)^{\frac{1}{m}} = B_1\left(\frac{1}{\lambda} - \frac{1}{\lambda_{gap}}\right) + B_2 \qquad eq.3$$

Where: λ_{gap} is the wavelength associated with the bandgap (nm); Abs is the absorption value (a.u.) at a given wavelength λ (nm); B_1 and B_2 are constants; m is the transition factor (m = 1/2 due to the presence of direct transitions) [14,68–71].

The value of $1/\lambda_{gap}$ was obtained by linear extrapolation of the $(Abs/\lambda)^{1/m}$ vs $1/\lambda$ plot [14,68–71]. After determining the value of $1/\lambda_{gap}$, the bandgap energy was calculated for every material using *Equation 4*.

$$E_{gap} = \frac{1240}{\lambda_{gap}} \qquad eq.4$$

Where: E_{gap} corresponds to the bandgap energy (eV) of the measured photocatalyst [14,68–71]. *Table 3* shows the results of the calculations for each of the materials synthesized.

Tab. 3 – Bandgap energy of all materials produced in this study

Material	**E_{gap} (eV)**	**Material**	**E_{gap} (eV)**
$BaSnO_3$ 900 °C	3.12	0.375CX/ZnO/$BaSnO_3$ 10 % 600°C	3.22
ZnO 600 °C	3.18	0.250CX/ZnO/$BaSnO_3$ 5 % 600 °C	3.22
0.375CX/ZnO 600 °C	3.21	0.500CX/ZnO/$BaSnO_3$ 5 % 600 °C	3.24
ZnO/$BaSnO_3$ 5 % 600 °C	3.21	0.375CX/ZnO/$BaSnO_3$ 5 % 300 °C	3.22
0.375CX/ZnO/$BaSnO_3$ 1 % 600 °C	3.22	0.375CX/ZnO/$BaSnO_3$ 5 % 400 °C	3.24
0.375CX/ZnO/$BaSnO_3$ 2.5 % 600 °C	3.22	0.375CX/ZnO/$BaSnO_3$ 5 % 500 °C	3.22
0.375CX/ZnO/$BaSnO_3$ 5 % 600 °C	3.22	0.375CX/ZnO/$BaSnO_3$ 5 % 700 °C	3.22
0.375CX/ZnO/$BaSnO_3$ 7.5 % 600 °C	3.22		

It can be noted from *Table 3* that ZnO exhibited a bandgap energy of 3.18 eV, whereas a 3.12 eV bandgap energy was obtained for the $BaSnO_3$, both in line with reported values [34,64]. For the ternary and binary composites, as expected, the bandgap values remained close to that of ZnO, ranging from 3.21-3.24 eV in all cases [22].

Furthermore, the energy values for the valence and conduction bands of ZnO and $BaSnO_3$ were determined based on their bandgap energies. For this purpose, *Equations 5 and 6* were applied to both semiconductors [55]:

$$E_{CB} = X - E^e - 0.5 \times E_{gap} \qquad eq.5$$

$$E_{VB} = E_{gap} + E_{CB} \qquad eq.6$$

Where: E_{CB} corresponds to the energy of the conduction band (eV); E_{VB} refers to the energy of the valence band (eV); X corresponds to the electronegativity of the semiconductor ($X_{ZnO} = 5.750\ eV$ e $X_{BaSnO_3} = 5.100\ eV$); E^e is the energy of free electrons vs. H_2, $E^e = 4.500\ eV$ [34,64].

Table 4 shows the results obtained for the valence and conduction bands for the unary materials ZnO and $BaSnO_3$.

Tab. 4 – Energy values for the bandgap, conduction, and valence band for the unary materials ZnO 600 °C and $BaSnO_3$ 900 °C

Materials	**E_{gap} (eV)**	**E_{CB} (eV)**	**E_{VB} (eV)**
ZnO 600 °C	3.18	-0.34	2.84
$BaSnO_3$ 900 °C	3.12	-0.96	2.16

The results shown in *Table 4* indicate a staggered band structure between the unary materials, which contributes to the formation of satisfactory heterojunctions (Z-scheme or type-II) in the ternary and binary composites.

To evaluate the morphological characteristics of the composites, *Figure 8* shows micrographs obtained through scanning electron microscopy for the ternary 0.375CX/ZnO/$BaSnO_3$ 5 % 600 °C, the binaries 0.375CX/ZnO 600 °C and ZnO/$BaSnO_3$ 5 % 600 °C, as well as the unaries ZnO 600 °C and $BaSnO_3$ 900 °C.

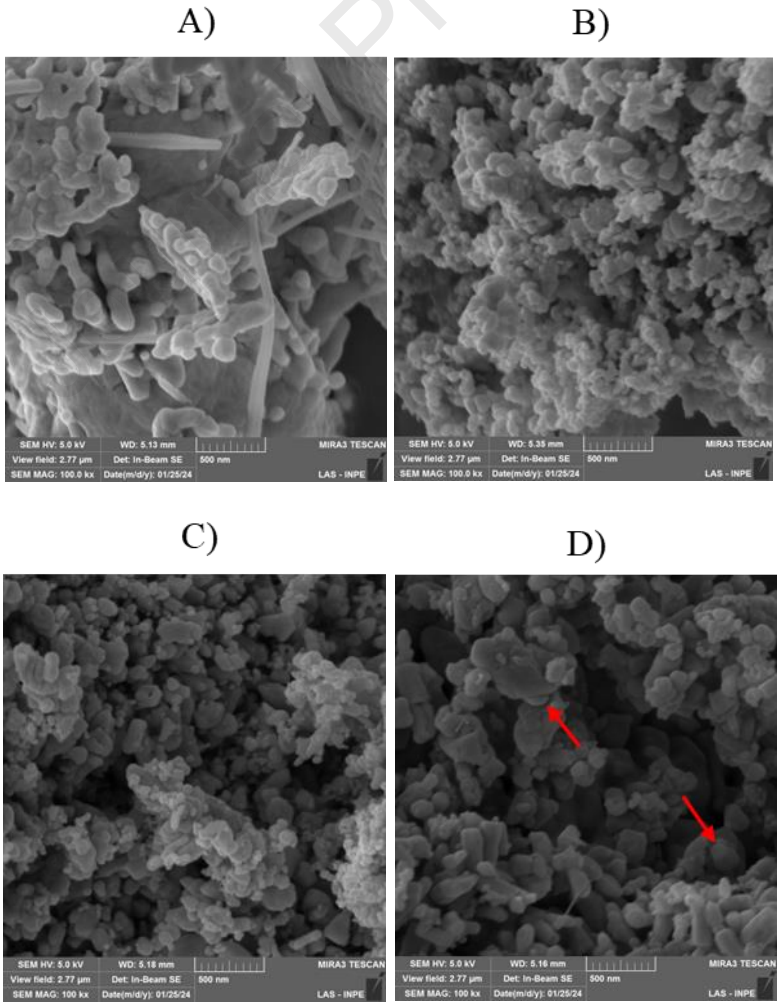

E)

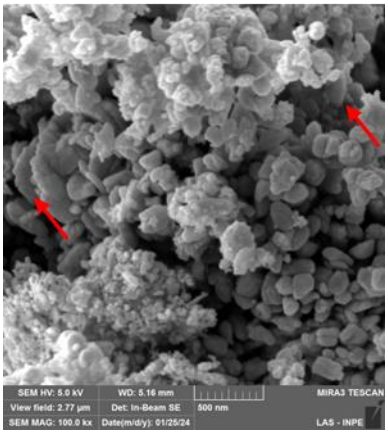

Fig. 8 – Scanning electron microscopy for the materials A) $BaSnO_3$ 900 °C (100000x); B) ZnO 600 °C (100000x); C) 0.375CX/ZnO 600 °C (100000x); D) ZnO/$BaSnO_3$ 5 % 600 °C (100000x); E) 0.375CX/ZnO/$BaSnO_3$ 5 % 600 °C (100000x);

Figure 8A shows that $BaSnO_3$ 900 °C consists of large plate-like particles and smaller irregular nodules, while *Figure 8B* reveals that ZnO 600 °C is composed of clusters of small nodular particles with a tendency towards sphericity, similar to what has been observed in the reported literature [61]. For the binary 0.375CX/ZnO 600 °C (*Figure 8C*), particles similar in shape and size to the unary ZnO were observed, contrasting with the characteristics displayed by the binary ZnO/$BaSnO_3$ 5 % 600 °C (*Figure 8D*) and ternary 0.375CX/ZnO/$BaSnO_3$ 5 % 600 °C (*Figure 8E*). Despite exhibiting nodular particles with a tendency towards sphericity of comparable dimensions to those of ZnO, these materials also demonstrated the formation of larger polyhedral particles (indicated by red arrows), potentially resulting from the incorporation of $BaSnO_3$ into their structure.

In order to evaluate the elemental distribution of the ternary 0.375CX/ZnO/$BaSnO_3$ 5 % 600 °C, the binaries 0.375CX/ZnO 600 °C and ZnO/$BaSnO_3$ 5 % 600 °C, and the unaries ZnO 600 °C and $BaSnO_3$ 900 °C, elemental mappings were obtained through energy-dispersive spectroscopy. The results are depicted in *Figure 9*.

A)

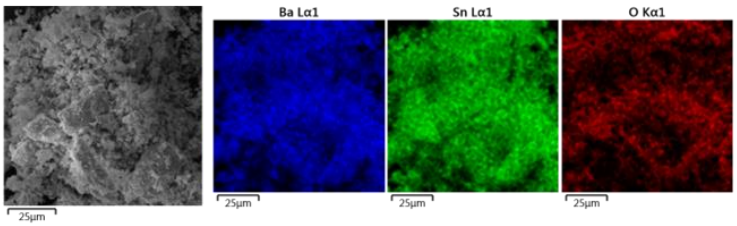

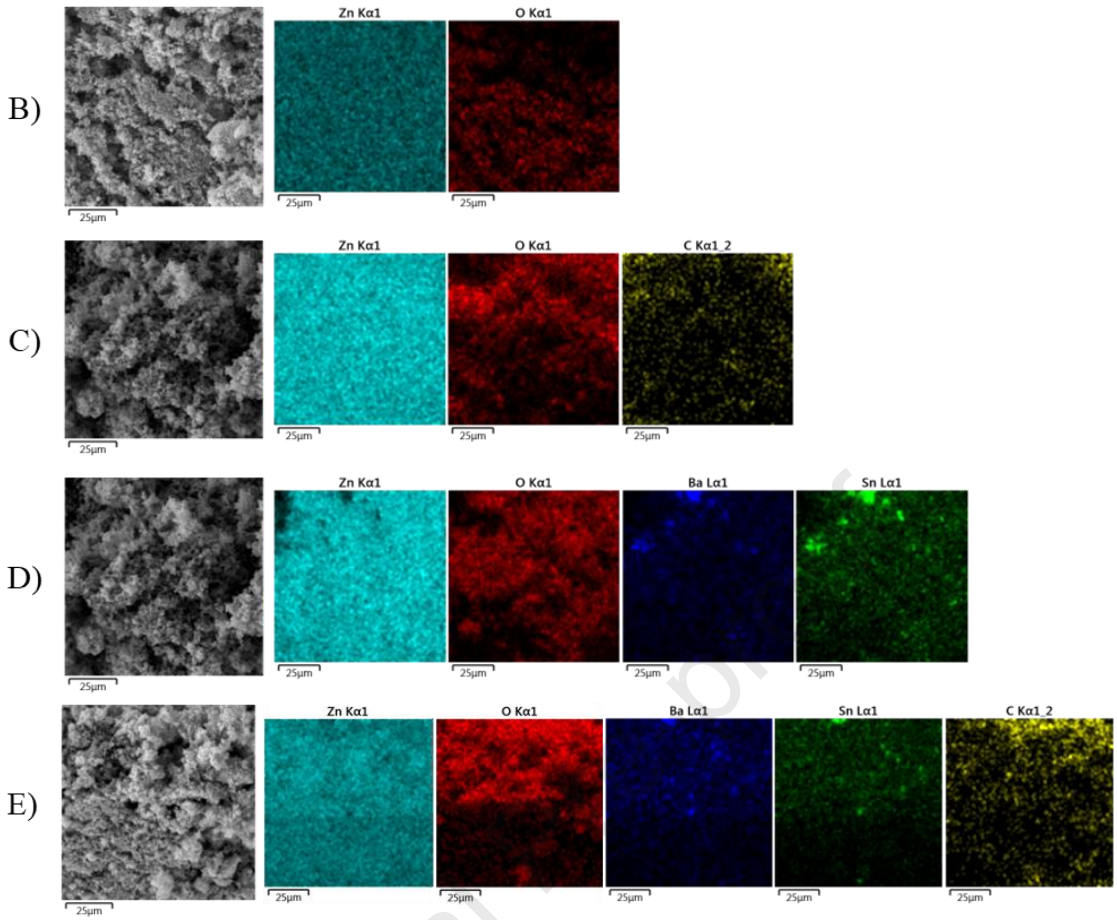

Fig. 9 – Micrographs and elemental distribution of the materials: A) $BaSnO_3$ 900 °C; B) ZnO 600 °C; C) 0.375CX/ZnO 600 °C; D) ZnO/$BaSnO_3$ 5 % 600 °C; E) 0.375CX/ZnO/$BaSnO_3$ 5 % 600 °C

Based on *Figures 9A, B, C, D, and E*, it can be observed that the elements composing all materials were well distributed on their surfaces, demonstrating the incorporation of the carbon xerogel and the barium stannate into their respective binary and ternary materials. This homogeneous distribution is advantageous for their photocatalytic abilities, facilitating charge transfer due to increased heterojunction availability within the materials, which can lower the rate of recombination between photogenerated charges, ultimately enhancing the efficiency of photodegradation [48,64,72,73].

For a more thorough evaluation of the material morphology, *Figures 10A, B, and C* respectively show the transmission electron micrographs and high-resolution transmission electron micrographs for $BaSnO_3$ 900 °C, ZnO 600 °C, and 0.375CX/ZnO/$BaSnO_3$ 5 % 600 °C.

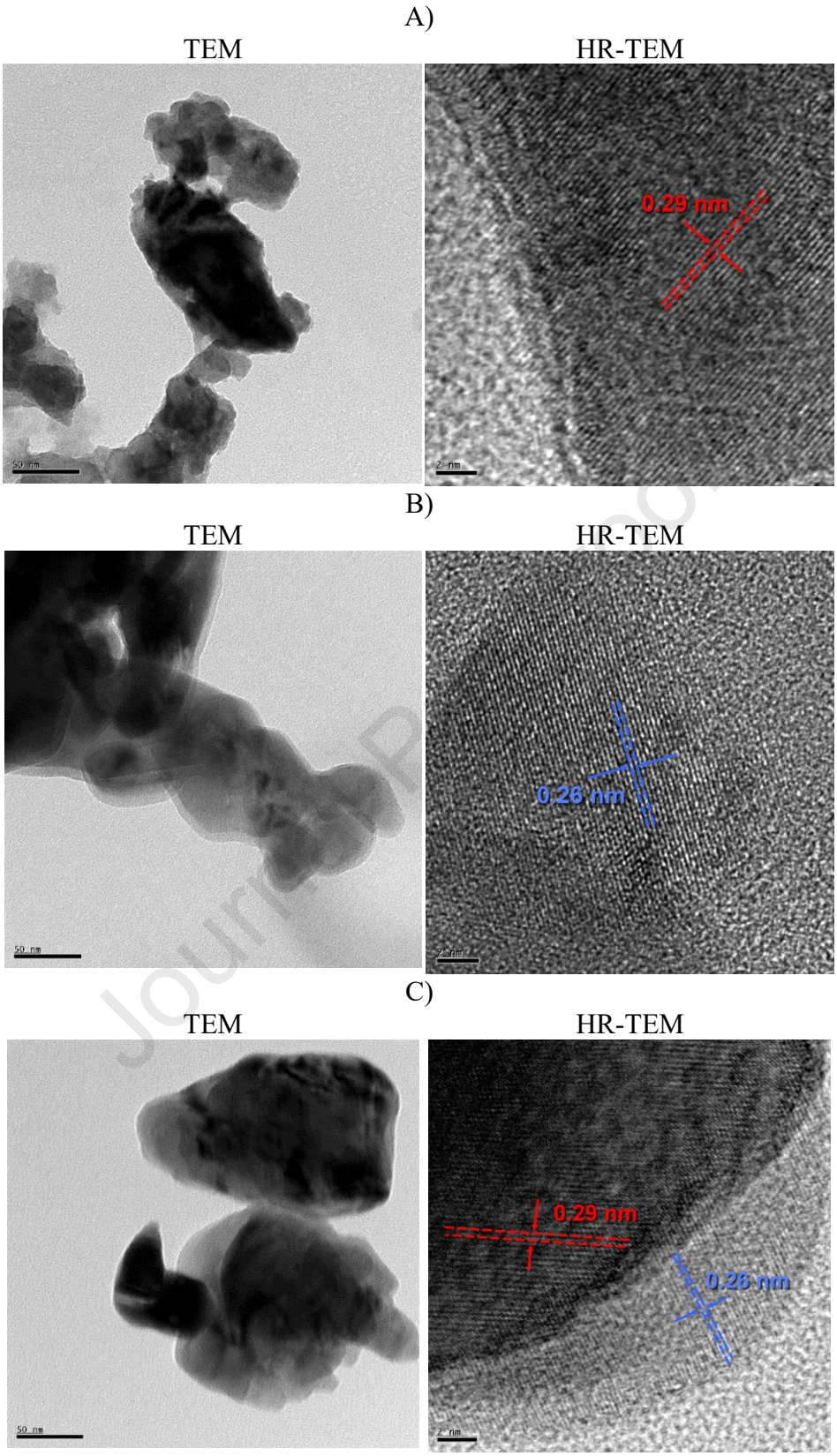

Fig. 10 – Trasmission electron micrographs (TEM) and high-resolution transmission electron micrographs (HR-TEM) for: A) $BaSnO_3$ 900 °C; B) ZnO; C) 0.375CX/ZnO/$BaSnO_3$ 5 % 600 °C

The TEM images of the materials reveal larger, irregularly shaped nodular and plate-like particles for $BaSnO_3$ 900 °C, while ZnO exhibits smaller, nodular particles with

a tendency towards sphericity. For the ternary material, nodular particles similar to ZnO in shape and size, were identified, while polyhedral nodular shapes corresponding to $BaSnO_3$ were also observed, in agreement with the results discussed for *Figure 8E*. HR-TEM analysis revealed a lattice spacing of 0.29 nm (in red) for both $BaSnO_3$ and the ternary material, corresponding to the (110) crystallographic plane of the $BaSnO_3$ perovskite, and a lattice spacing of 0.26 nm (in blue) was observed in ZnO and the ternary material, referring to the (002) plane typical of the hexagonal phase of ZnO. These findings align with the XRD results shown in *Figure 4*, further corroborating the presence of both ZnO and $BaSnO_3$ in the ternary system [50,74].

Figures 11A, B, and Table 5 show, respectively, the adsorption-desorption isotherms, the pore size distribution, and the morphological parameters obtained for the ternary 0.375CX/ZnO/$BaSnO_3$ 5 % 600 °C, the binaries 0.375CX/ZnO 600 °C and ZnO/$BaSnO_3$ 5 % 600 °C and the unaries ZnO 600 °C and $BaSnO_3$ 900 °C.

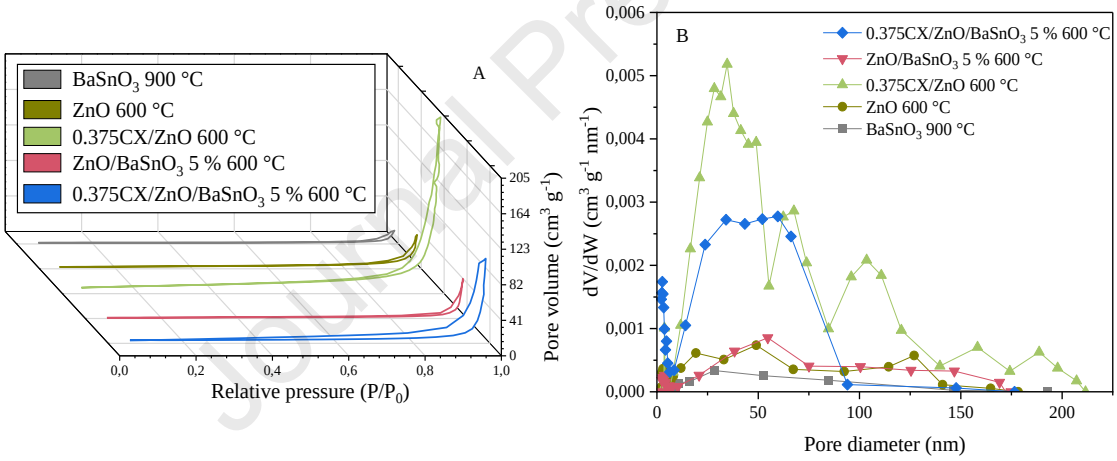

Fig. 11 – A) N_2 adsorption-desorption isotherms; B) Pore diameter distribution for the materials: $BaSnO_3$ 900 °C; ZnO 600 °C; 0.375CX/ZnO 600 °C; ZnO/$BaSnO_3$ 5 % 600 °C; 0.375CX/ZnO/$BaSnO_3$ 5 % 600 °C

Tab. 5 – Morphological parameters for the ternary 0.375CX/ZnO/$BaSnO_3$ 5 % 600 °C compared to their respective binaries 0.375CX/ZnO 600 °C, ZnO/$BaSnO_3$ 5 % 600 °C, and unaries ZnO 600 °C and $BaSnO_3$ 900 °C

Material	Specific surface area ($m^2\ g^{-1}$)	Micropore area ($m^2\ g^{-1}$)	Pore volume ($cm^3\ g^{-1}$)	Micropore volume ($cm^3\ g^{-1}$)
ZnO 600 °C	8.241	3.459	0.310	0.004
$BaSnO_3$ 900 °C	4.371	-	0.024	-
0.375CX/ZnO 600 °C	29.914	8.164	0.315	0.004
ZnO/$BaSnO_3$ 5 % 600 °C	3.431	1.183	0.071	0.001
0.375CX/ZnO/$BaSnO_3$ 5 % 600 °C	12.351	9.482	0.151	0.005

It was observed that the isotherms obtained for all materials can be classified as type IV-H3, according to the International Union of Pure and Applied Chemistry (IUPAC) (*Figure 11A*). The type IV isotherm classification is typical of mesoporous materials, while the H3 hysteresis corresponds to clusters of small particles with pores in the form of slits and irregular internal openings [15,48]. In addition, according to *Table 5*, there was a significant increase of almost 4 times in the surface area and 2 times in the pore volume for the 0.375CX/ZnO/$BaSnO_3$ 5 % 600 °C in comparison to the binary ZnO/$BaSnO_3$ 5 % 600 °C. This tendency was also acknowledged when comparing the binary 0.375CX/ZnO 600 °C with unary ZnO 600 °C, in which case there was a more than 3-fold increase in the surface area of the binary and a slight increase in pore volume (0.005 $cm^3\ g^{-1}$), showcasing the positive impact of carbon xerogel on the morphology of the materials. The observed increase in surface area could be beneficial for the photocatalytic activity of the materials due to the larger area available for the propagation of reactions involved in the photocatalytic process [48,64].

However, when comparing the ternary 0.375CX/ZnO/$BaSnO_3$ 5 % 600 °C with the binary 0.375CX/ZnO 600 °C, it was possible to identify a decrease in both the surface area and pore volume and an increase in the percentage of micropore area relative to total surface area (76.8 % for ternary *vs.* 27.3 % for binary) and the volume of micropores relative to total volume (3.3 % for ternary *vs*. 1.3 % for binary). This tendency can be explained by possible obstruction of carbon xerogel meso and macropores with $BaSnO_3$ particles, in agreement with the apparent larger particle size of this photocatalyst observed

in the SEM and TEM micrographs (*Figure 8A and 10A*) [39,48]. Moreover, $BaSnO_3$ 900 °C exhibited low surface area and pore volume, lacking significant results for micropore surface area and micropore volume, which may lead to poorer photocatalytic activity.

Based on *Figure 11B*, when comparing both materials containing carbon xerogel to the binary ZnO/$BaSnO_3$ 5 % 600 °C and the unary materials, it can be inferred that the addition of carbon xerogel resulted in an enhanced porous structure, encompassing both meso and microporous regions, as anticipated [49]. The binary 0.375CX/ZnO 600 °C showed a higher concentration of pores ranging from 10 nm to 120 nm in diameter; for the ternary 0.375CX/ZnO/$BaSnO_3$ 5 % 600 °C, there was a higher concentration of pores with diameters smaller than 10 nm and between 10 nm and 90 nm, consistent with the potential blockage of pores with larger diameters by $BaSnO_3$.

Finally, *Figure 12* displays the results of the chronoamperometry tests conducted to assess the photocurrent generation of the ternary 0.375CX/ZnO/$BaSnO_3$ 5 % 600 °C in comparison to the binaries 0.375CX/ZnO 600 °C and ZnO/$BaSnO_3$ 5 % 600 °C, as well as the unary materials ZnO 600 °C and $BaSnO_3$ 900 °C.

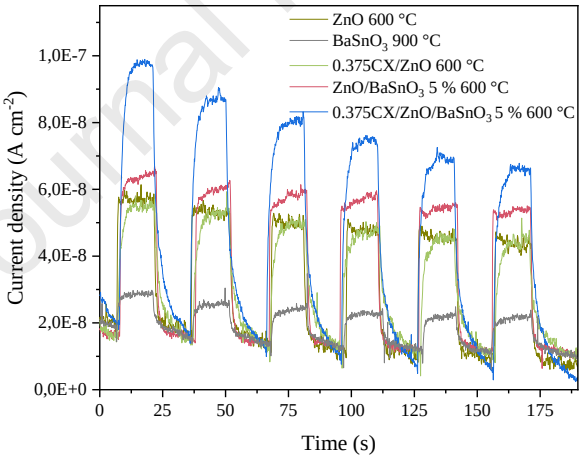

Fig. 12 – Chronoamperometry test results using the best ternary (0.375CX/ZnO/$BaSnO_3$ 5 % 600 °C) and its binary (ZnO/$BaSnO_3$ 5 % 600 °C, 0.375CX/ZnO 600 °C) and unary (ZnO 600 °C, $BaSnO_3$ 900 °C) counterparts, under simulated solar radiation

Analysis of *Figure 12* reveals that the ternary 0.375CX/ZnO/$BaSnO_3$ 5 % 600 °C exhibited the highest photocurrent generation capacity, indicating its potential superiority as a photocatalyst. This outcome can be attributed to several factors, including the possible reduction in charge recombination rates, increased sensitization to a broader range of the visible spectra, and improved charge transfer facilitated by the addition of $BaSnO_3$ and carbon xerogel to the system [15,22,39].

The charge transfer resistance of the 0.375CX/ZnO/$BaSnO_3$ 5 % 600 °C material was evaluated in comparison to the binary systems 0.375CX/ZnO 600 °C and ZnO/$BaSnO_3$ 5 % 600 °C, as well as the unary materials ZnO 600 °C and $BaSnO_3$ 900 °C. For that purpose, electrochemical impedance spectroscopy was performed under solar radiation for the materials and in the absence of light for the ternary material, as shown in *Figure 13*. Furthermore, circuits based on the Randles model were simulated for each material, as indicated in *Table S1* (with R_s representing the resistance of the solution between working and reference electrodes, R_{ct} charge transfer resistance, and C_{dl} double-layer capacitance in a non-ideal constant phase element-CPE). The CPE equivalent circuits in impedance (Z_{cpe}) measurements can represented with *Equation 7* [75,76]:

$$Z_{cpe} = (C_{dl}(jw)^n)^{-1} \qquad eq.7$$

Where: C_{dl} represents pseudo-capacitance, whose electrochemical nature has been described earlier; n is a constant ranging from 0 to 1, where a rough or porous surface may cause a double layer with a n value between 0.5 and 1; j is the imaginary number ($j^2 = -1$); w is the angular frequency (rad s^{-1}) [76].

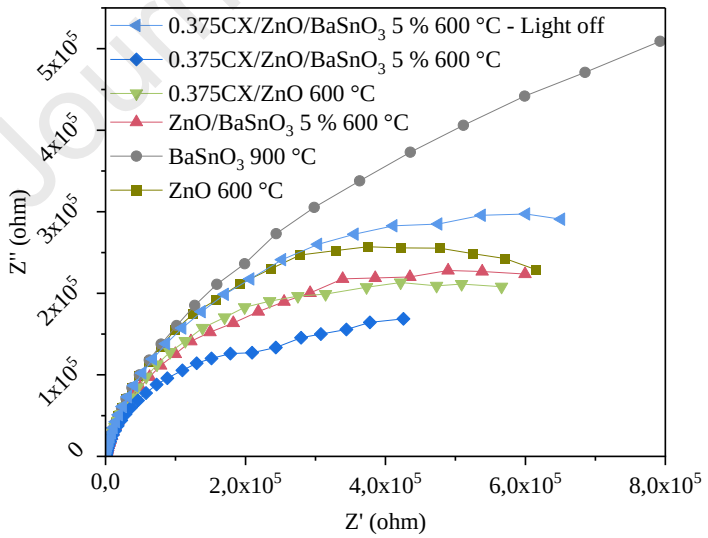

Fig. 13 - Nyquist plots obtained from electrochemical impedance spectroscopy under solar irradiation for the materials 0.375CX/ZnO/$BaSnO_3$ 5 % 600 °C, ZnO/$BaSnO_3$ 5 % 600 °C, 0.375CX/ZnO 600 °C, ZnO 600 °C, and $BaSnO_3$ 900 °C and without illumination for the 0.375CX/ZnO/$BaSnO_3$ 5 % 600 °C

Figure 13 reveals a distinct difference in the arc radii for the ternary 0.375CX/ZnO/$BaSnO_3$ 5 % 600 °C material, both with and without simulated solar light irradiation. This significant reduction in charge transfer resistance under solar light

confirms the material's photoactivity, which is also supported by chronoamperometry tests conducted under solar radiation. Additionally, when comparing the arc radii of the materials exposed to solar radiation, the ternary system demonstrated the lowest charge transfer resistance, indicating more efficient separation of photogenerated charges during the photocatalytic process, which suggests the effectiveness of the heterojunction potentially formed within the system. The other arcs displayed a similar trend to that observed in the chronoamperometry results [22,60,75]. Furthermore, as shown in *Table S1*, all simulated circuits exhibited values of x^2 equal to or smaller than the order of 10^{-3}, validating the accuracy of the simulations; the values obtained for the charge transfer resistance are in accordance with what was observed in the Nyquist plot (*Figure 13*), with the lowest value observed for the ternary material (266290 Ω) [75,76].

3.2. Photocatalytic evaluation

Firstly, the photocatalytic tests for the materials with variation in $BaSnO_3$ content (1-10 %) were conducted. This evaluation is depicted in *Figures 14A and B*, corresponding to SA degradation under solar and visible radiation, respectively.

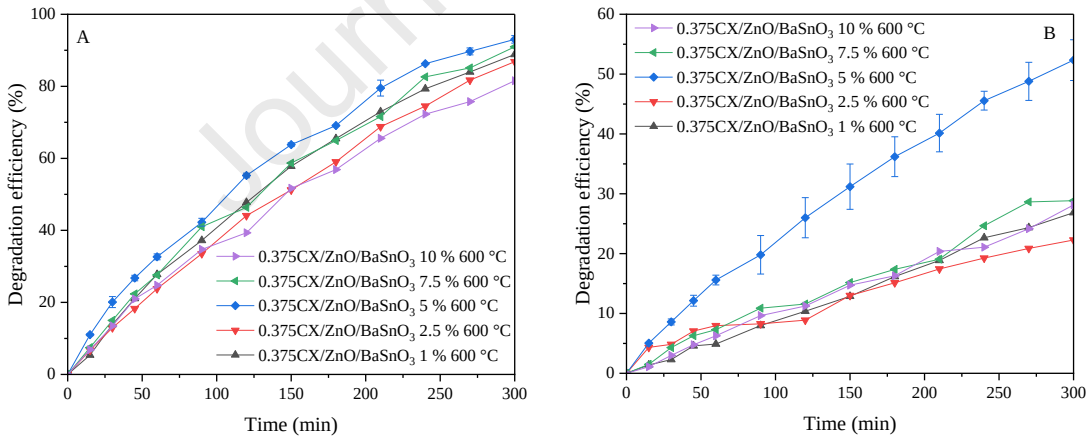

Fig. 14 – Results of photocatalytic tests for the degradation of SA (10 mg L^{-1}) using the ternaries 0.375CX/ZnO/$BaSnO_3$ 600 °C with different quantities of $BaSnO_3$ (1-10 %) under A) Solar; B) Visible radiation

It was noted from *Figures 14A and B* that, for both solar and visible radiation, the material that presented the best results (93.0 % solar, 52.3 % visible radiation) in SA degradation was the 0.375CX/ZnO/$BaSnO_3$ 5 % 600 °C. These results can be related to the possible formation of heterojunctions between ZnO, $BaSnO_3$, and the carbonaceous

matrix, promoting more efficient charge separation on the conduction and valence bands with greater redox ability, facilitating the generation of active radicals responsible for the degradation of SA. Despite the good effect caused by the addition of $BaSnO_3$ to the structure, as its mass increased in the system, the crystallite sizes of the materials also increased (*Table 2*), showing that the best photocatalytic efficiency observed for the ternary with 5 % w/w of $BaSnO_3$ was a consequence of several factors interacting in the structure of the developed photocatalysts [54,55].

Afterward, based on the best performance observed for the material with 5 % w/w $BaSnO_3$ content, a study was carried out to evaluate the influence of the added amount of tannin (0.250-0.500 g) on the photocatalytic efficiency of the ternaries, as shown in *Figures 15A and B*.

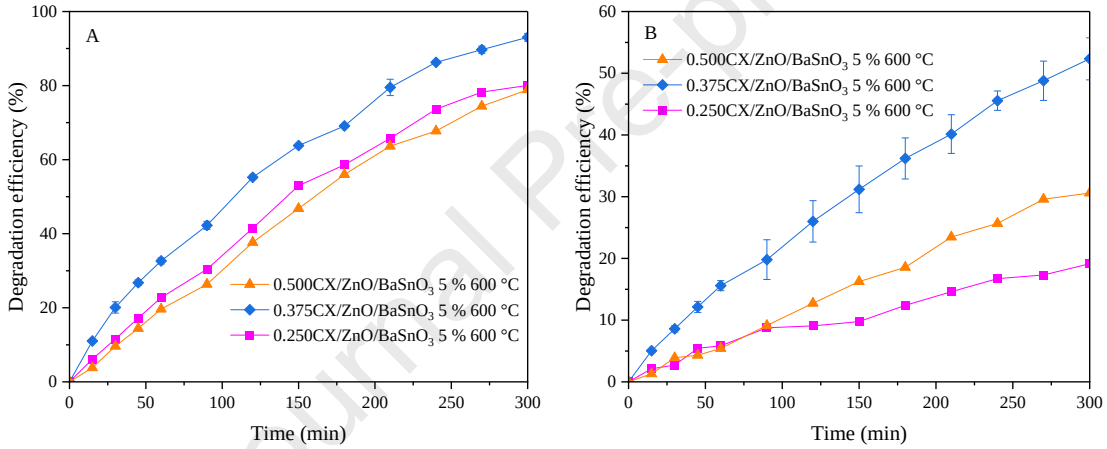

Fig. 15 – Results of photocatalytic tests for the degradation of SA (10 mg L^{-1}) using the ternaries CX/ZnO/$BaSnO_3$ 5 % 600 °C with different quantities of added tannin (0.25-0.50 g) under A) Solar; B) Visible radiation

Figures 15A and B show that the material that presented the best results was the 0.375CX/ZnO/$BaSnO_3$ 5 % 600 °C, under both solar and visible radiation, showcasing the influence of the amount of tannin added on the photocatalytic activity of the hybrid photocatalysts. These results can be explained by the fact that greater amounts of added tannin may have led to insufficient amounts of semiconductors in the system, decreasing the availability of heterojunctions formed, whereas lower amounts of tannin may have negatively affected the absorbance at longer wavelengths and led to materials with larger crystallite sizes (in agreement with what was discussed for the characterizations by XRD and diffuse reflectance spectroscopy), impairing the photocatalytic activity [14,39,49,54,55].

Based on the results obtained, the amount of tannin added was set at 0.375 g for the ternary system. The effect of the calcination temperature on the photocatalytic activity of the photocatalysts (300-700 °C) was then evaluated. *Figures 16A and B* show the results obtained under solar and visible radiation, respectively.

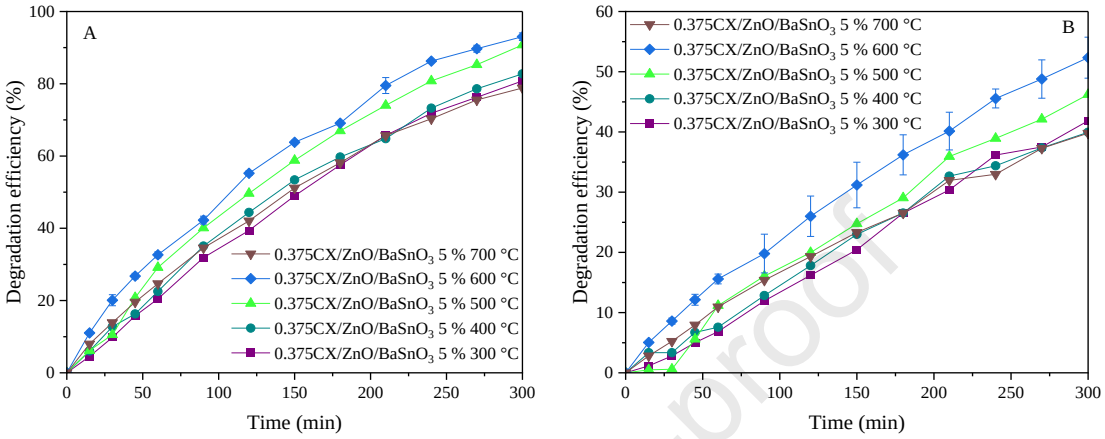

Fig. 16 – Results of photocatalytic tests for the degradation of SA (10 mg L^{-1}) using the ternaries 0.375CX/ZnO/$BaSnO_3$ 5 % with different calcination temperatures (300-700 °C) under A) Solar; B) Visible radiation

The results shown in *Figures 16A and B* indicate that 0.375CX/ZnO/$BaSnO_3$ 5 % 600 °C had the best SA degradation both under solar and visible radiation. The best material in both radiations was calcined at 600 °C, followed by the material calcined at 500 °C, demonstrating the favorable effect of higher calcination temperatures on the properties of the photocatalysts, especially on their absorbance at longer wavelengths, as observed in their characterization by diffuse reflectance spectroscopy [14,39,49]. Furthermore, it is reported that the increase in calcination temperature results in an increase in the degree of graphitization of the carbon xerogel in the structure, leading to higher electrical conductivities and, consequently, better transfer of photogenerated charges and enhanced photocatalytic activities [77,78]. However, the ternary photocatalyst calcined at 700 °C deviated from the expected trend, likely due to its relatively large crystallite size, as indicated in *Table 2*. This increased crystallite size, compared to other ternary photocatalysts subjected to different calcination temperatures, may account for its lower photocatalytic activity [54,55].

Thus, the ternary 0.375CX/ZnO/$BaSnO_3$ 5 % 600 °C was selected as the material with the best photocatalytic activity among all ternary materials, being chosen for subsequent studies. *Figures 17A and B* compare the photocatalytic activity of the ternary photocatalyst with its corresponding binary and unary counterparts. For the ternary

photocatalyst, the evaluation of the SA photodegradation was also carried out using an HPLC, as shown in *Figures 17C and D* for the tests under solar and visible radiation, respectively.

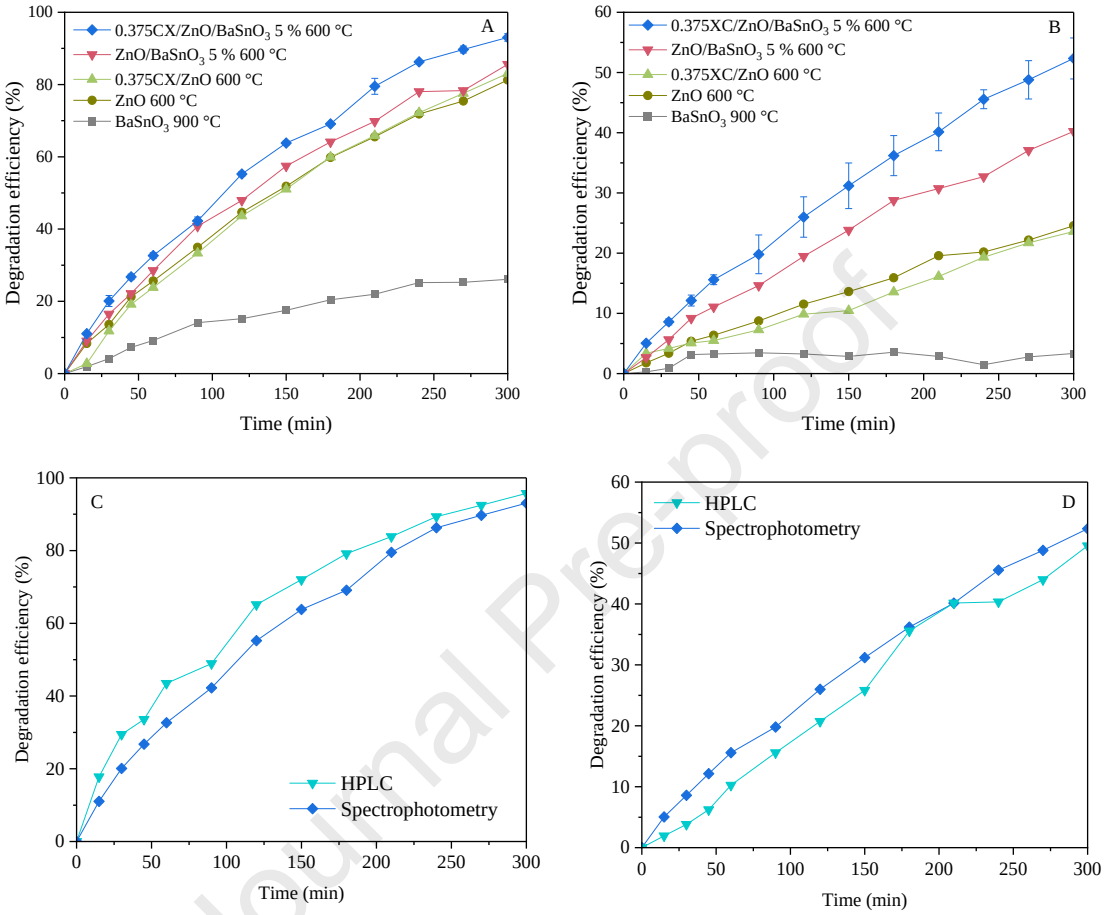

Fig. 17 – Results of photocatalytic tests for the degradation of SA (10 mg L^{-1}) using the best ternary (0.375CX/ZnO/$BaSnO_3$ 5 % 600 °C) and its binary (ZnO/$BaSnO_3$ 5 % 600 °C, 0.375CX/ZnO 600 °C) and unary (ZnO 600 °C, $BaSnO_3$ 900 °C) counterparts under A) Solar; B) Visible radiation and the HPLC results for the degradation of SA (10 mg L^{-1}) using 0.375 CX/ZnO/$BaSnO_3$ 5 % 600 °C under C) Solar and D) Visible radiation

The results depicted in *Figures 17A and B* show that the SA degradation efficiency followed the same order (worst to best) for both solar and visible radiation: $BaSnO_3$ 900 °C; ZnO 600 °C and 0.375CX/ZnO 600 °C (similar results); ZnO/$BaSnO_3$ 5 % 600 °C; 0.375CX/ZnO/$BaSnO_3$ 5 % 600 °C (93.0 % degradation under solar radiation and 52.3 % under visible radiation). The lower efficiency observed for the $BaSnO_3$ can be explained by its high recombination rate and low sensitivity to visible radiation [32]. The ZnO 600 °C, on the other hand, exhibited results comparable to the 0.375CX/ZnO 600 °C, which can be attributed to their similar photocurrent generation capacity (*Figure 12*)

and ZnO's effective activation under the UV component of solar radiation and potential creation of isolated defect states below the ZnO conduction band, explaining its photocatalytic response in the visible region, consistent with its absorption capacity between 400 and 500 nm observed in its diffuse reflectance spectra (*Figure 7D*) [22]. The ZnO/$BaSnO_3$ 5 % composite demonstrated slightly lower efficiency compared to the ternary system, agreeing with results from the chronoamperometry and electrochemical impedance tests (*Figure 12 and 13*), suggesting that the interaction between ZnO and $BaSnO_3$ promotes the formation of efficient heterojunctions, contributing to enhanced photocatalytic activity. However, the absence of a solid-state mediator in this composite, along with a larger crystallite size (*Table 2*), may have contributed to its reduced efficiency, potentially due to the formation of less efficient heterojunctions when compared to the ternary system [54,55].

Therefore, the photocatalyst which exhibited the best degradation efficiency results, both under solar and visible radiation, was the ternary 0.375CX/ZnO/$BaSnO_3$ 5 % 600 °C, consistent with the findings from the extensive characterization conducted:

- XRD: Smaller crystallite sizes were observed for the materials with carbon addition, leading to better photocatalytic activities [54,55];
- Diffuse reflectance spectroscopy: Sensitization to visible radiation due to the addition of carbon xerogel [22,61];
- N_2 adsorption-desorption isotherms and BET analysis: Increase in pore volume compared to ZnO/$BaSnO_3$ 5 % 600 °C and surface area compared to materials without carbon addition, allowing for better propagation of photocatalytic effects. [48,64];
- EDS: Homogeneous distribution of elements, enabling good availability of heterojunctions and leading to a lower rate of recombination of photogenerated charges [48,64,72];
- Chronoamperometry: Higher photocurrent generation capacity compared to binaries and unaries, resulting in better photocatalytic activity [15,39].
- Electrochemical impedance spectroscopy: Lower charge transfer resistance, indicating a more efficient separation of photogenerated charges [22,60,75].

Furthermore, *Figures 17C and D* reveal that the degradation results obtained via HPLC closely align with those acquired through spectrophotometry. This indicates that

the formation of degradation by-products did not significantly impact the proposed measurement methodology.

To better describe the behavior of the photocatalytic tests performed, the kinetic parameters of each photodegradation reaction were calculated. Typically, the Langmuir-Hinshelwood (L-H) model is satisfactorily used for photocatalytic reactions. *Equation 8* represents the simplified format commonly employed in related literature [48].

$$\mathrm{Ln}\left(\frac{C_0}{C}\right) = k_r \times K_{ad} \times t = k_{app} \times t \qquad eq.8$$

Where: C corresponds to the concentration of the compound being measured at a given time (t); k_r refers to the specific velocity of the photocatalytic reaction; K_{ad} is the adsorption coefficient; C_0 corresponds to the initial concentration; k_{app} is the apparent reaction rate constant [48].

Thus, the simplified format of the L-H model was used to determine the kinetic parameters of the SA photodegradation reactions under both solar and visible radiation, as shown in *Table 6*.

Tab. 6 – Kinetic parameters of the photocatalytic reactions under solar and visible radiation using all the materials produced in this work

Material	Solar radiation		Visible radiation	
	$k_{app\ (min^{-1})}$	R^2	$k_{app\ (min^{-1})}$	R^2
$BaSnO_3$ 900 °C	0.0010	0.965	-	-
ZnO 600 °C	0.0054	0.995	0.0009	0.996
0.375CX/ZnO 600 °C	0.0057	0.991	0.0008	0.983
ZnO/$BaSnO_3$ 5 % 600 °C	0.0061	0.986	0.0017	0.996
0.375CX/ZnO/$BaSnO_3$ 1 % 600 °C	0.0070	0.986	0.0011	0.996
0.375CX/ZnO/$BaSnO_3$ 2.5 % 600 °C	0.0064	0.974	0.0008	0.978
0.375CX/ZnO/$BaSnO_3$ 5 % 600 °C	0.0085	0.978	0.0024	0.999
0.375CX/ZnO/$BaSnO_3$ 7.5 % 600 °C	0.0075	0.970	0.0011	0.984
0.375CX/ZnO/$BaSnO_3$ 10 % 600 °C	0.0054	0.990	0.0011	0.994
0.250CX/ZnO/$BaSnO_3$ 5 % 600 °C	0.0056	0.992	0.0007	0.983
0.500CX/ZnO/$BaSnO_3$ 5 % 600 °C	0.0052	0.990	0.0013	0.994
0.375CX/ZnO/$BaSnO_3$ 5 % 300 °C	0.0055	0.991	0.0019	0.993
0.375CX/ZnO/$BaSnO_3$ 5 % 400 °C	0.0058	0.991	0.0018	0.994
0.375CX/ZnO/$BaSnO_3$ 5 % 500 °C	0.0075	0.981	0.0021	0.994
0.375CX/ZnO/$BaSnO_3$ 5 % 700 °C	0.0052	0.997	0.0017	0.997

The results in *Table 6* show that the L-H model is appropriate to describe the behavior of the tests performed since R^2 values were close to 1 in all cases. In line with the photocatalytic tests, the material that presented the highest k_{app}, under both radiations evaluated, was the 0.375CX/ZnO/$BaSnO_3$ 5 % 600 °C (0.0085 min^{-1} for solar and 0.0024 min^{-1} for visible radiation), confirming its superior photocatalytic efficiency when compared to all materials tested in this study (the k_{app} constant could not be determined for the $BaSnO_3$ under visible radiation, due to its low photocatalytic activity – *Figure 17B*).

Furthermore, an assessment of total organic carbon removal was also conducted for the best ternary photocatalyst and its corresponding binary and unary materials, showcasing the mineralization capacity of salicylic acid for each material. The results obtained are shown in *Figure 18* (the assessment was not performed for the $BaSnO_3$ 900 °C due to its low degradation efficiency, as previously observed in *Figures 17A and B*).

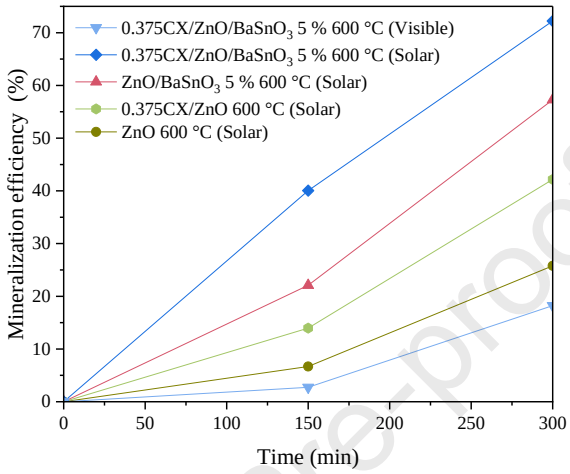

Fig. 18 – Results of mineralization obtained through the evaluation of total organic carbon for the degradation of SA (10 mg L^{-1}) using the best ternary (0.375CX/ZnO/$BaSnO_3$ 5 % 600 °C) and its binary (ZnO/$BaSnO_3$ 5 % 600 °C, 0.375CX/ZnO 600 °C) and unary (ZnO 600 °C) counterparts under solar radiation and, for the best ternary, also under visible radiation

Figure 18 shows that the ternary photocatalyst presented the best mineralization capacity of SA amongst the tested materials, with a mineralization efficiency of 72.2 % under solar radiation. Furthermore, the mineralization efficiency followed the same trend observed for the materials in *Figures 17A and B*, underscoring that the proposed photocatalysts are not only effective in degrading the SA molecule but also in facilitating its complete mineralization. Additionally, it is possible to conclude that the mineralization efficiency increased in accordance with the increase in degradation efficiency, indicating that these processes can progress synchronously [79]. Finally, in a similar way to the degradation process, the mineralization achieved with the ternary photocatalyst under visible light was significantly lower than that observed under solar radiation. This can be attributed to the broader range of wavelengths in the solar spectrum, including UV light, which enhances photocatalytic activation and thereby improves mineralization efficiency. [80].

After being identified as the most effective material for the degradation and mineralization of SA, the ternary 0.375CX/ZnO/$BaSnO_3$ 5 % 600 °C was tested to

investigate the mechanism of active radical generation in the photocatalytic reaction, as depicted in *Figure 19*.

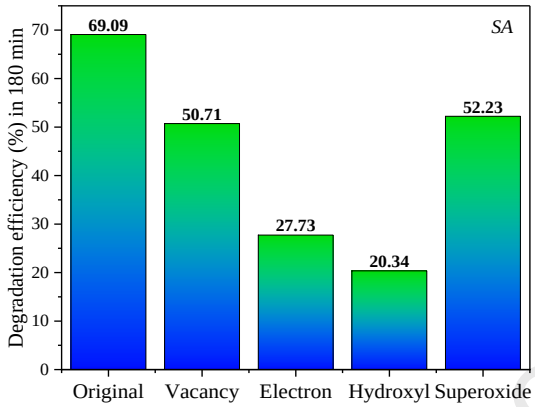

Fig. 19 – Results for SA (10 mg L^{-1}) photodegradation with the best ternary (0.375CX/ZnO/$BaSnO_3$ 5 % 600 °C) using suppressors

The findings from *Figure 19* indicate that the hydroxyl radical had the most pronounced impact on the photodegradation reaction, with its suppression resulting in a 48.8 % decrease in degradation efficiency. Furthermore, the electron also played a significant role in the degradation process, leading to a 41.4 % reduction in degradation efficiency when suppressed. Electron holes and superoxide radicals also contributed to degradation efficiency, albeit to a lesser degree. *Equations 9-15* present a potential mechanism for the generation of active radicals during the photodegradation reaction [22,61,81,82]:

$$Photocatalyst + \lambda \rightarrow e^- + h^+ \qquad eq.9$$

$$H_2O + h^+ \rightarrow \cdot OH + H^+ \qquad eq.10$$

$$O_2 + e^- \rightarrow O_2^{\cdot -} \qquad eq.11$$

$$\cdot OH + \cdot OH \rightarrow H_2O_2 \qquad eq.12$$

$$e^- + O_2^{\cdot -} + 2H^+ \rightarrow H_2O_2 \qquad eq.13$$

$$e^- + H_2O_2 \rightarrow \cdot OH + OH^- \qquad eq.14$$

$$H_2O_2 + O_2^{\cdot -} \rightarrow \cdot OH + O_2 + OH^- \qquad eq.15$$

The significant impact of hydroxyl radicals on SA degradation, as shown in *Figure 19*, elucidates the influence of the pathway described in *Equation 12*, which involves the generation of hydroxyl radicals through the oxidation of adsorbed water by electron holes created during photonic excitation. Additionally, the significant influence of

photogenerated electrons and the minor effect of superoxide radicals suggest the involvement of the pathway described in *Equation 11*, leading to pollutant degradation either directly by superoxide or, more likely, by the formation of additional hydroxyl radicals, as indicated by *Equations 13-15*. The surprisingly subtle influence of the electron hole suppression can be explained by the reduction in recombination rates of the e^-/h^+ pair, resulting in a higher electron concentration, promoting hydroxyl radical generation through the pathway described by *Equations 11 and 13-15*, thereby compensating for the lack of hydroxyl radicals generated through the pathway described by *Equation 10* [22].

Moreover, based on the data from *Table 4*, a Z-type heterojunction formation between ZnO and $BaSnO_3$ was proposed for the ternary material (*Figure 20*), aligning with the staggered band structure of these compounds, the notable photocurrent generation capability, lower charge-transfer resistance for the material, and the discussed photodegradation results. For the described ternary system, carbon xerogel likely served as a solid-state mediator to facilitate the recombination of charges with lower redox potential between ZnO (CB = -0.34 eV) and $BaSnO_3$ (VB = 2.16 eV), preserving photogenerated electrons in the conduction band of $BaSnO_3$ (CB = -0.96 eV) and electron holes in the valence band of ZnO (VB = 2.84 eV). Consequently, the preserved electron hole in the valence band of ZnO can cause the oxidation of adsorbed water molecules (E^0 = 2.70 eV), fostering the formation of hydroxyl radicals. Similarly, the photogenerated electrons in the conduction band of $BaSnO_3$ may reduce adsorbed oxygen into superoxide radicals (E^0 = -0.28 eV), consistent with the results discussed for suppressor tests performed (*Figure 19*) [15,22,64,83,84].

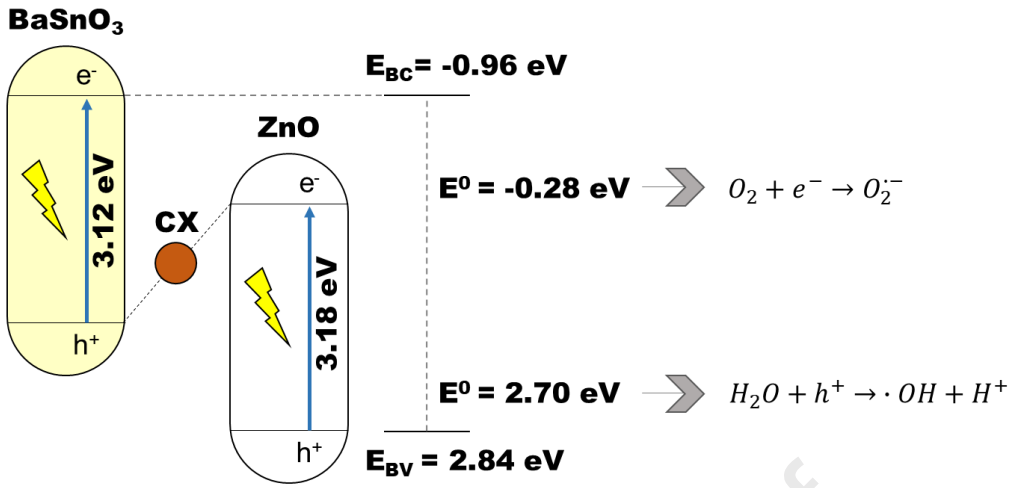

Fig. 20 - Z-type heterojunction proposed between ZnO and $BaSnO_3$, with carbon xerogel as a solid-state mediator

Figure 21 and *Table 7* display, respectively, the photographs and the results of measurements conducted for the assessment of the phytotoxicity of the post-treatment solutions obtained using the optimized ternary catalyst (under solar and visible radiation) compared to the initial standard SA solution of 10 mg L^{-1} and the control solution of deionized water.

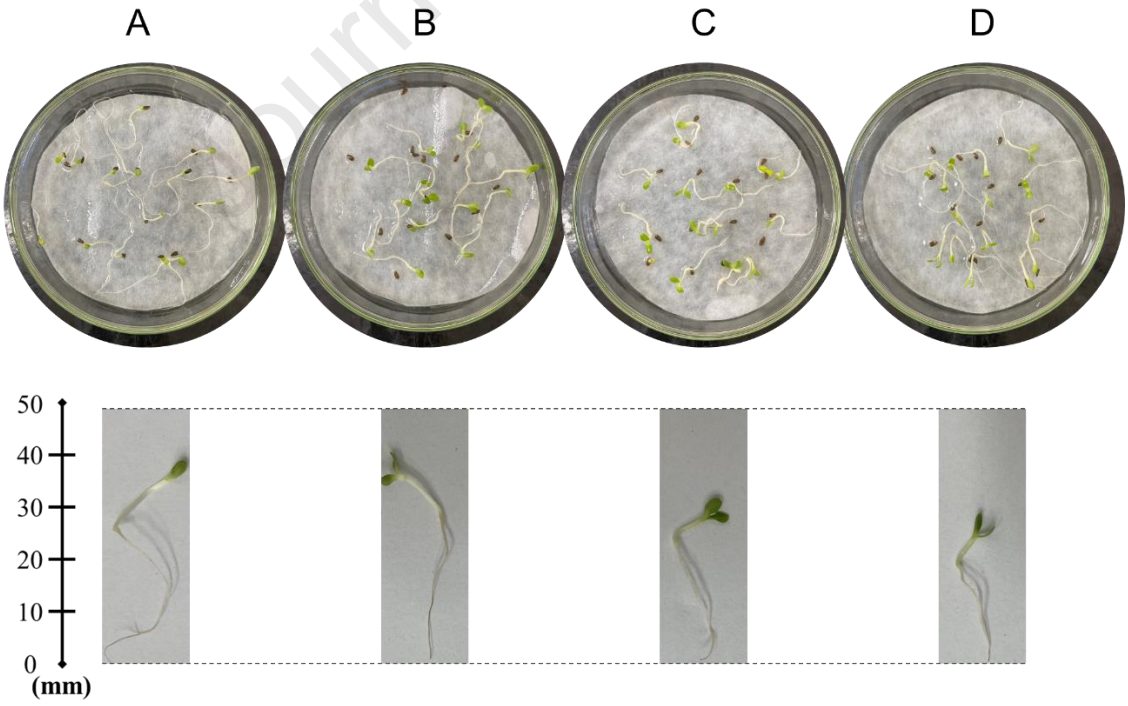

Fig. 21 - *Lactuca sativa* assays after a 4-day period of incubation: A) Deionized water (control); B) SA solution after degradation using 0.375CX/ZnO/$BaSnO_3$ 5 % 600 °C under solar radiation; C) SA solution after degradation using 0.375CX/ZnO/$BaSnO_3$ 5 % 600 °C under visible radiation; D) SA initial solution 10 mg L^{-1}

Tab. 7 - Mean values of root length (mm), shoot length, and total length of lettuce seedlings subjected to different solutions.

Solutions	Root length (mm)	Shoot length (mm)	Total length (mm)
Deionized water (control)	33.86 ± 3.2 [a]	11.35 ± 2.8 [a]	45.22 ± 4.2 [a]
0.375CX/ZnO/$BaSnO_3$ 5 % 600 °C - Solar radiation	30.19 ± 5.4 [a]	8.97 ± 1.7 [b]	39.19 ± 5.2 [b]
0.375CX/ZnO/$BaSnO_3$ 5 % 600 °C - Visible radiation	21.58 ± 2.7 [b]	7.65 ± 1.5 [b]	29.23 ± 3.2 [c]
SA initial solution 10 mg L^{-1}	16.61 ± 1.6 [c]	7.66 ± 1.3 [b]	24.27 ± 2.6 [d]

Note: Mean values followed by the same letters, on the same column, do not differ significantly from each other according to the Tukey test ($p > 0.05$)

Based on the graphical representation of seedlings in *Figure 21* and *Tables S2, S3, S4, and S5*, and the data in *Table 7* and *Figure S1*, it was observed that the control group showed the highest growth rate in root length, leading to an increase in total plant length, consistent with expectations. Subsequently, the group of seedlings exposed to the post-treatment solution employing the 0.375CX/ZnO/$BaSnO_3$ 5 % 600 °C photocatalyst under solar radiation exhibited the second-best results for these metrics, in line with the enhanced mineralization of the SA solution under solar radiation (*Figure 18*), which may have resulted in decreased xenobiotic concentrations and consequently reduced toxicity. Conversely, the group exposed to the solution treated under visible radiation showed inferior performance compared to the aforementioned group across all variables, highlighting the superior degradation and mineralization efficiency of the pollutant under solar radiation, in line with observations in *Figures 17A and B, and Figure 18*.

Notably, a more pronounced disparity in root growth was observed, whereas, for shoot growth, the results were comparable, apart from the control group. This heightened root sensitivity in *Lactuca sativa* has been previously reported and aligns with the fact that the root is the first organ to come into contact with substances in the environment and the primary system responsible for the intake and accumulation of substances in the plant [85,86]. Lastly, as expected, the group exposed to the untreated pollutant solution exhibited the poorest growth in both root and total length, further underscoring the detrimental effects of *Lactuca sativa*'s exposure to salicylic acid.

Finally, *Figures 22A, B, C, and D* show the degradation efficiency results of SA using the ternary 0.375CX/ZnO/$BaSnO_3$ 5 % 600 °C, by varying the SA concentration (2.5-50 mg L^{-1}), salinity (0-30 g_{NaCl} L^{-1}), pH (2.9-9.3), and photocatalyst mass (0.05-0.20 g), respectively. Furthermore, *Table 8* presents the kinetic data obtained using the Langmuir-Hinshelwood (L-H) model (*Equation 8*) for each of the tests conducted.

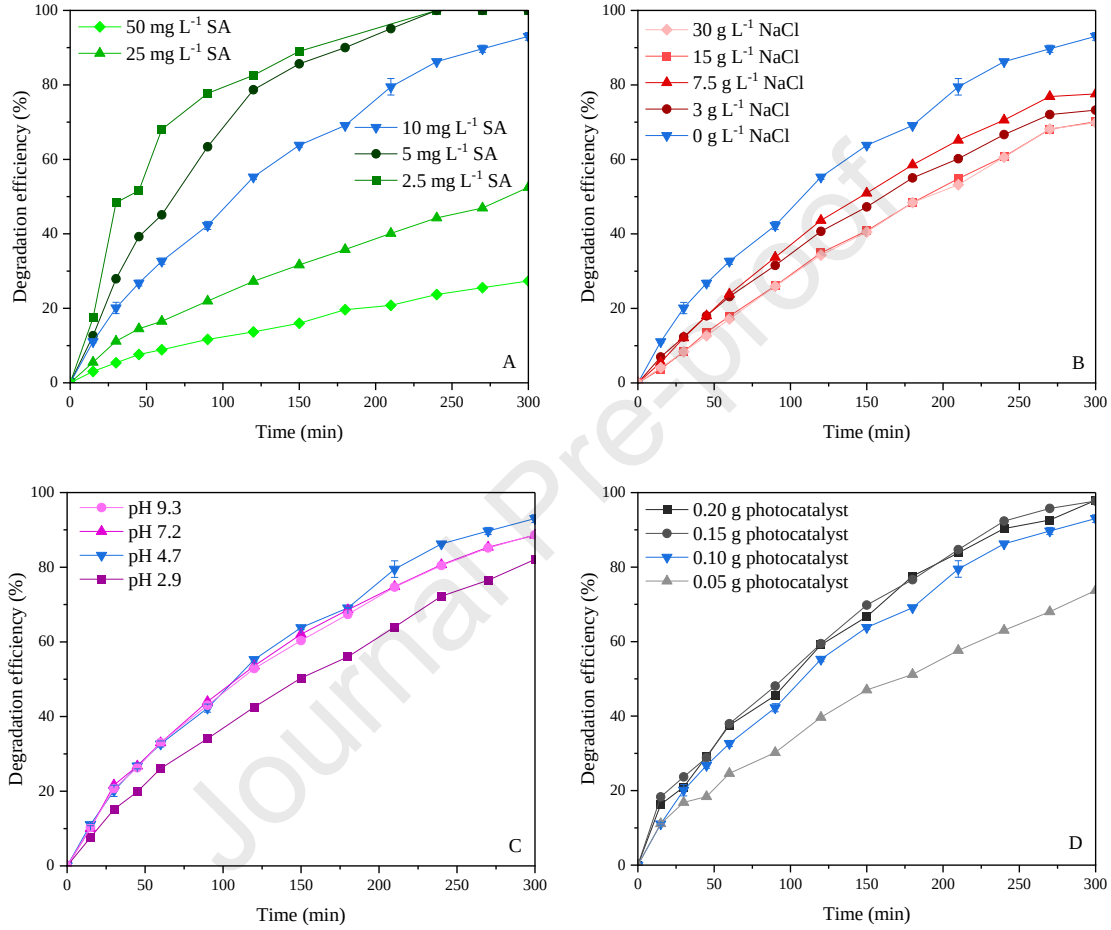

Fig. 22 **-** Results of photocatalytic tests for the degradation of SA using the best ternary (0.375CX/ZnO/$BaSnO_3$ 5 % 600 °C) under solar radiation with variation of: A) SA concentration (2.5-50 mg L^{-1}, maintaining pH 4.7, photocatalyst mass at 0.1 g, and NaCl concentration at 0 g L^{-1}), B) *Salinity* (0-30 g_{NsCl} L^{-1}, maintaining SA concentration at 10 mg L^{-1}, pH 4.7, and photocatalyst mass at 0.1 g), C) pH (2.9-9.3, maintaining SA concentration at 10 mg L^{-1}, photocatalyst mass at 0.1 g, and NaCl concentration at 0 g L^{-1}), and D) *Photocatalyst* mass (0.05-0.20 g, maintaining SA concentration at 10 mg L^{-1}, pH 4.7, and NaCl concentration at 0 g L^{-1})

Tab. 8 - Kinetic parameters of the photocatalytic reactions under solar radiation using 0.375CX/ZnO/$BaSnO_3$ 5 % 600 °C with variations in reaction parameters

SA conc. (mg L^{-1})	NaCl conc. (g L^{-1})	Solution pH	Photocatalyst mass (g)	k_{app} (min^{-1})	R^2
10*	0*	4.7*	0.10*	0.0085	0.978
2.5	0	4.7	0.10	0.0117	0.946
5	0	4.7	0.10	0.0140	0.989
25	0	4.7	0.10	0.0023	0.992
50	0	4.7	0.10	0.0010	0.991
10	3	4.7	0.10	0.0045	0.997
10	7.5	4.7	0.10	0.0052	0.996
10	15	4.7	0.10	0.0041	0.993
10	30	4.7	0.10	0.0041	0.991
10	0	2.9	0.10	0.0054	0.986
10	0	7.2	0.10	0.0070	0.994
10	0	9.3	0.10	0.0070	0.992
10	0	4.7	0.05	0.0041	0.993
10	0	4.7	0.15	0.0106	0.949
10	0	4.7	0.20	0.0094	0.978

Note: * Reaction standard conditions

Firstly, *Table 8* clearly indicates that all reactions adhered to the L-H model, with R^2 values close to one. Furthermore, *Figure 22A* and *Table 8* demonstrate a decline in both degradation efficiency and k_{app} as the concentration of the pollutant SA increased. Since the ternary photocatalyst did not exhibit significant adsorption of the pollutant in any of the tests, it is likely that the generation of active radicals for pollutant degradation occurred via the adsorption of H_2O molecules on its surface. Since the photocatalyst quantity was held constant while the SA concentration varied, a similar number of active species would be generated irrespective of pollutant concentration. This could explain the observed decrease in degradation efficiency as the SA concentration increased [87]. Additionally, according to *Figure 22B* and *Table 8*, a tendency for reduced degradation efficiency and a decline in k_{app} was observed with an increased NaCl concentration in the system. This can be explained by the scavenging effect of Na^+ and Cl^- ions on hydroxyl radicals, which play a crucial role in SA degradation, as shown in *Figure 19*.

Consequently, the higher concentration of these ions in the system hindered the overall efficiency of the process [45,88,89].

Regarding *Figure 22C* and *Table 8*, it was observed that the lowest degradation efficiency and k_{app} were found at the most acidic pH (pH 2.9), which may be explained by the partial dissolution of ZnO present in the photocatalyst at this pH [90]. From pH 4.7 onward, there was no significant change in degradation efficiency, which can be attributed to the lack of adsorption of SA molecules on the photocatalyst in any of the experiments, suggesting that potential changes in the overall charge of the photocatalyst particles with pH variation did not affect the degradation process [45]. This outcome is advantageous considering the process's application.

Finally, *Figure 22D* and *Table 8* clearly demonstrate that varying the photocatalyst mass had a significant impact on both degradation efficiency and k_{app}, with higher masses resulting in better efficiency and increased rate constants. This can be explained by the greater availability of active species responsible for SA degradation, as their generation is directly proportional to the amount of photocatalyst in the system. However, this effect was most evident when the mass increased from 0.05 g to higher amounts, as further increases caused the solution to become more turbid, hindering the photocatalytic process [91,92].

4. Conclusion

Initially, based on the characterization results, it can be concluded that all synthesized materials exhibited the desired components in their structures, validating the synthesis routes proposed. Through the process of parameter optimization for the CX/ZnO/$BaSnO_3$ ternary system, it was observed that the content of $BaSnO_3$, the amount of added tannin, and the calcination temperature influenced the properties and photocatalytic activity of the materials; the parameters that yielded the best results for the ternary system were: 5 % w/w $BaSnO_3$ content, 0.375 g of added tannin, and a calcination temperature of 600 °C. Photocatalytic tests confirmed the superiority of the ternary system, demonstrating higher degradation of SA under solar (93.0 %) and visible radiation (52.3 %), as well as superior SA mineralization (72.2 %) under solar radiation. Moreover, it was identified that hydroxyl radicals have the greatest influence on the photodegradation process, followed by photogenerated electrons. The formation of a Z-type heterojunction was proposed for the composite, given the staggered band alignment

observed for the ZnO and $BaSnO_3$ and the potential role of carbon xerogel as a solid-state electronic mediator, facilitating efficient separation of photogenerated charges. The phytotoxicity tests confirmed the favorable growth rate of *Lactuca sativa* organisms when subjected to SA solutions treated with 0.375CX/ZnO/$BaSnO_3$ 5 % 600 °C under solar radiation, thereby evidencing the reduction in the overall toxicity of the solution. Finally, variations in pH, photocatalyst mass, SA concentration, and salinity significantly affected the degradation efficiency of SA when utilizing the 0.375CX/ZnO/$BaSnO_3$ 5 % 600 °C photocatalyst under solar radiation. The ternary system demonstrated high degradation efficiency over a broad pH range, with a more pronounced decrease at the lowest tested pH (2.9) and a clear increase in efficiency as more photocatalyst was added, particularly when increasing the mass from 0.05 g to higher amounts during SA photodegradation (10 mg L^{-1}). Furthermore, even at elevated salinity levels (30 g L^{-1}), the material sustained good degradation efficiency (>60 %) for SA and proved to be particularly effective for pollutant concentrations below 10 mg L^{-1}.

Credit authorship contribution statement

Flávio Henrique Covolam Boldrin: Formal analysis, Investigation, Methodology, Validation, Visualization, Writing - original draft, Writing - review & editing. **Laila Gazel de Andrade**: Formal analysis, Investigation, Methodology, Validation, Visualization, Writing - original draft. **Ikaro Tessaro**: Formal analysis, Investigation, Methodology, Validation, Visualization, Writing - original draft **Bruno Henrique Baena da Silva:** Formal analysis, Investigation, Methodology, Validation, Visualization, Writing - original draft. **Robson da Silva Souto**: Formal analysis, Investigation, Methodology, Validation, Visualization, Writing - original draft. **Nicolas Perciani de Moraes**: Formal analysis, Investigation, Methodology, Software, Supervision, Validation, Visualization, Writing - original draft, Writing - review & editing. **Robson da Silva Rocha**: Formal analysis, Investigation, Methodology, Software, Supervision, Validation, Visualization, Writing - original draft, Writing - review & editing. **Marcos Roberto de Vasconcelos Lanza:** Formal analysis, Funding acquisition, Investigation, Methodology, Software, Supervision, Validation, Visualization, Writing - original draft, Writing - review & editing. **Liana Alvares Rodrigues**: Formal analysis, Funding acquisition, Investigation, Methodology, Project administration, Software,

Supervision, Validation, Visualization, Writing - original draft, Writing - review & editing.

Declaration of competing interest

The authors declare that they have no known competing financial interests or personal relationships that could have appeared to influence the work reported in this paper.

Data availability

Data will be made available on request.

Acknowledgments

The authors would like to thank the Coordenação de Aperfeiçoamento de Pessoal de Nivel Superior - Brasil (CAPES) - Financing Code 001, the São Paulo Research Foundation – FAPESP (Grants #2023/12207-0, #2022/12895-1 and #2022/04058-2) and the National Council for Scientific and Technological Development - CNPq (Grants #303943/2021-1 and #308576/2022-5) for the financial support. The authors are also grateful to TANAC S.A., which supplied the black wattle tannin (PHENOTAN AP).

References

[1] T. Liu, C.O. Aniagor, M.I. Ejimofor, M.C. Menkiti, K.H.D. Tang, B.L.F. Chin, Y.H. Chan, C.L. Yiin, K.W. Cheah, Y. Ho Chai, S.S.M. Lock, K.L. Yap, M.X.J. Wee, P.-S. Yap, Technologies for removing pharmaceuticals and personal care products (PPCPs) from aqueous solutions: Recent advances, performances, challenges and recommendations for improvements, J. Mol. Liq. 374 (2023) 121144. https://doi.org/10.1016/j.molliq.2022.121144.

[2] N.K. Stamatis, I.K. Konstantinou, Occurrence and removal of emerging pharmaceutical, personal care compounds and caffeine tracer in municipal sewage treatment plant in Western Greece, J. Environ. Sci. Heal. - Part B Pestic.

Food Contam. Agric. Wastes. 48 (2013) 800–813. https://doi.org/10.1080/03601234.2013.781359.

[3] V. Kavitha, Global prevalence and visible light mediated photodegradation of pharmaceuticals and personal care products (PPCPs)-a review, Results Eng. 14 (2022). https://doi.org/10.1016/j.rineng.2022.100469.

[4] E.N. Evgenidou, I.K. Konstantinou, D.A. Lambropoulou, Occurrence and removal of transformation products of PPCPs and illicit drugs in wastewaters: A review, Sci. Total Environ. 505 (2015) 905–926. https://doi.org/10.1016/j.scitotenv.2014.10.021.

[5] M.J.M. Bueno, M.J. Gomez, S. Herrera, M.D. Hernando, A. Agüera, A.R. Fernández-Alba, Occurrence and persistence of organic emerging contaminants and priority pollutants in five sewage treatment plants of Spain: Two years pilot survey monitoring, Environ. Pollut. 164 (2012) 267–273. https://doi.org/10.1016/j.envpol.2012.01.038.

[6] Y. Yang, Y.S. Ok, K.H. Kim, E.E. Kwon, Y.F. Tsang, Occurrences and removal of pharmaceuticals and personal care products (PPCPs) in drinking water and water/sewage treatment plants: A review, Sci. Total Environ. 596–597 (2017) 303–320. https://doi.org/10.1016/j.scitotenv.2017.04.102.

[7] R.G. Ciocarlan, H. Wang, B. Cuypers, M. Mertens, Y. Wu, S. Van Doorslaer, E.M. Seftel, P. Cool, ZnTi layered double hydroxides as photocatalysts for salicylic acid degradation under visible light irradiation, Appl. Clay Sci. 197 (2020). https://doi.org/10.1016/j.clay.2020.105757.

[8] M.K. Arfanis, P. Adamou, N.G. Moustakas, T.M. Triantis, A.G. Kontos, P. Falaras, Photocatalytic degradation of salicylic acid and caffeine emerging contaminants using titania nanotubes, Chem. Eng. J. 310 (2017) 525–536. https://doi.org/10.1016/j.cej.2016.06.098.

[9] Gangwang, G. Liu, H. Liu, N. Zhang, Y. Wang, Photodegradation of salicylic acid in aquatic environment: Effect of different forms of nitrogen, Sci. Total Environ. 435–436 (2012) 573–577. https://doi.org/10.1016/j.scitotenv.2012.05.068.

[10] C. Byrne, G. Subramanian, S.C. Pillai, Recent advances in photocatalysis for

environmental applications, J. Environ. Chem. Eng. 6 (2018) 3531–3555. https://doi.org/10.1016/j.jece.2017.07.080.

[11] S. Ahmed, F.S.A. Khan, N.M. Mubarak, M. Khalid, Y.H. Tan, S.A. Mazari, R.R. Karri, E.C. Abdullah, Emerging pollutants and their removal using visible-light responsive photocatalysis – A comprehensive review, J. Environ. Chem. Eng. 9 (2021). https://doi.org/10.1016/j.jece.2021.106643.

[12] X. Li, Y. Bai, X. Shi, N. Su, G. Nie, R. Zhang, H. Nie, L. Ye, Applications of MXene ($Ti_3C_2T_X$) in photocatalysis: A review, Mater. Adv. 2 (2021) 1570–1594. https://doi.org/10.1039/d0ma00938e.

[13] G. Vilé, Photocatalytic materials and light-driven continuous processes to remove emerging pharmaceutical pollutants from water and selectively close the carbon cycle, Catal. Sci. Technol. 11 (2021) 43–61. https://doi.org/10.1039/d0cy01713b.

[14] N.P. de Moraes, L.A. Bacetto, G.S. dos Santos, M.L.C. Pinto da Silva, J.P.B. Machado, T.M.B. Campos, G.P. Thim, L.A. Rodrigues, Synthesis of novel ZnO/carbon xerogel composites: Effect of carbon content and calcination temperature on their structural and photocatalytic properties, Ceram. Int. 45 (2019) 3657–3667. https://doi.org/10.1016/j.ceramint.2018.11.027.

[15] N.P. de Moraes, T.M.B. Campos, G.P. Thim, A. de Siervo, M.R. de V. Lanza, L.A. Rodrigues, Application of a new lignin/cellulose carbon xerogel/ZnO/Bi_2O_3/Bi° composite photocatalyst for the degradation of bisphenol-A under sunlight, Chem. Phys. Impact. 6 (2023) 100182. https://doi.org/10.1016/j.chphi.2023.100182.

[16] S.A. Mahmoud, O.A. Fouad, Synthesis and application of zinc/tin oxide nanostructures in photocatalysis and dye sensitized solar cells, Sol. Energy Mater. Sol. Cells. 136 (2015) 38–43. https://doi.org/10.1016/j.solmat.2014.12.035.

[17] S.A. Mirsalari, A. Nezamzadeh-Ejhieh, A.R. Massah, A designed experiment for CdS-AgBr photocatalyst toward methylene blue, Environ. Sci. Pollut. Res. 29 (2022) 33013–33032. https://doi.org/10.1007/s11356-021-17569-1.

[18] A.N. Ejhieh, M. Khorsandi, Photodecolorization of Eriochrome Black T using NiS–P zeolite as a heterogeneous catalyst, J. Hazard. Mater. 176 (2010) 629–637.

https://doi.org/10.1016/j.jhazmat.2009.11.077.

[19] S.G. Kumar, K.S.R.K. Rao, Zinc oxide based photocatalysis: Tailoring surface-bulk structure and related interfacial charge carrier dynamics for better environmental applications, RSC Adv. 5 (2015) 3306–3351. https://doi.org/10.1039/c4ra13299h.

[20] L. Daneshvar, A. Nezamzadeh-Ejhieh, Photocatalytic activity of ZnO nanoparticles towards tinidazole degradation: Experimental design by response surface methodology (RSM), Desalin. Water Treat. 141 (2019) 364–376. https://doi.org/10.5004/dwt.2019.23310.

[21] R.T. Sapkal, S.S. Shinde, T.R. Waghmode, S.P. Govindwar, K.Y. Rajpure, C.H. Bhosale, Photo-corrosion inhibition and photoactivity enhancement with tailored zinc oxide thin films, J. Photochem. Photobiol. B Biol. 110 (2012) 15–21. https://doi.org/10.1016/j.jphotobiol.2012.02.004.

[22] M.E.V. Gouvea, F.H.C. Boldrin, B.H.B. da Silva, L.K. Paiva, N.P. de Moraes, L. Gonçalves de Aguiar, L.A. Rodrigues, Fluidized bed reactor for 4-chlorophenol photodegradation via solar and visible radiation using ZnO/g-C_3N_4/carbon xerogel as a photocatalyst, Chem. Phys. Impact. 8 (2024) 100428. https://doi.org/10.1016/j.chphi.2023.100428.

[23] A. Yousefi, A. Nezamzadeh-Ejhieh, Preparation and characterization of SnO_2-$BiVO_4$-CuO catalyst and kinetics of phenazopyridine photodegradation, Iran. J. Catal. 11 (2021) 247–259.

[24] M. Rezaei, A. Nezamzadeh-Ejhieh, A.R. Massah, A comprehensive review on the boosted effects of anion vacancy in the heterogeneous photocatalytic degradation, part I: Focus on sulfur, nitrogen, carbon, and halogen vacancies, Ecotoxicol. Environ. Saf. 269 (2024) 115927. https://doi.org/10.1016/j.ecoenv.2024.115927.

[25] M. Rezaei, A. Nezamzadeh-Ejhieh, A.R. Massah, A Comprehensive Review on the Boosted Effects of Anion Vacancy in the Photocatalytic Solar Water Splitting: Focus on Sulfur Vacancy, Energy & Fuels. 38 (2024) 7637–7664. https://doi.org/10.1021/acs.energyfuels.4c00325.

[26] H. Zhang, Z. Wang, J. Zhang, K. Dai, Metal-sulfide-based heterojunction

photocatalysts: Principles, impact, applications, and in-situ characterization, Chinese J. Catal. 49 (2023) 42–67. https://doi.org/10.1016/S1872-2067(23)64444-4.

[27] M. Foroughipour, A. Nezamzadeh-Ejhieh, $CaTiO_3$ perovskite /g-C_3N_4 heterojunction-based composite photocatalyst, part II: Synthesis, characterization and the boosted photocatalytic activity towards Gemifloxacin, Diam. Relat. Mater. 141 (2024) 110711. https://doi.org/10.1016/j.diamond.2023.110711.

[28] M. Foroughipour, A. Nezamzadeh-Ejhieh, $CaTiO_3$/g-C_3N_4 heterojunction-based composite photocatalyst: Part I: Experimental design, kinetics, and scavenging agents' effects in photocatalytic degradation of gemifloxacin, Chemosphere. 334 (2023) 139019. https://doi.org/10.1016/j.chemosphere.2023.139019.

[29] T. Li, A. Jiang, Y. Di, D. Zhang, X. Zhu, L. Deng, X. Ding, S. Chen, Novel $BaSnO_3$/TiO_2@HNTs Heterojunction Composites with Highly Enhanced Photocatalytic Activity and Stability, ChemistrySelect. 6 (2021) 10817–10826. https://doi.org/10.1002/slct.202102834.

[30] X. Chen, Q. Dong, S. Chen, Z. Zhang, X. Zhang, Y. Di, A. Jiang, D. Zhang, T. Li, Halloysite nanotubes supported $BiVO_4$/$BaSnO_3$ p-n heterojunction photocatalysts for the enhanced degradation of methylene blue under visible light, Colloids Surfaces A Physicochem. Eng. Asp. 664 (2023) 131143. https://doi.org/10.1016/j.colsurfa.2023.131143.

[31] X. Chen, Z. Zhang, S. Chen, Q. Dong, X. Zhang, Y. Di, A. Jiang, D. Zhang, T. Li, Synthesis of halloysite nanotubes supported Bi-modified $BaSnO_3$ photocatalysts for the enhanced degradation of methylene blue under visible light, Opt. Mater. (Amst). 134 (2022) 113202. https://doi.org/10.1016/j.optmat.2022.113202.

[32] A.A. Baoum, A.A. Ismail, Enhanced photocatalytic efficiency of highly effective and stable perovskite $BaSnO_3$ with monoclinic Li_2MnO_3 nanoparticles: Atrazine a case study of herbicide, Ceram. Int. 49 (2023) 23227–23237. https://doi.org/10.1016/j.ceramint.2023.04.152.

[33] N. Rajamanickam, P. Soundarrajan, K. Jayakumar, K. Ramachandran, Improve the power conversion efficiency of perovskite BaSnO3 nanostructures based dye-

sensitized solar cells by Fe doping, Sol. Energy Mater. Sol. Cells. 166 (2017) 69–77. https://doi.org/10.1016/j.solmat.2017.03.021.

[34] I.A. Mkhalid, S.I. El-Hout, S-scheme $AgVO_3$-decorated $BaSnO_3$ heterojunction for efficient photoreduction of Mercury (II) ions under visible light, J. Taiwan Inst. Chem. Eng. 146 (2023) 104896. https://doi.org/10.1016/j.jtice.2023.104896.

[35] Y. Zhao, J. Ma, J. Liu, Y. Bao, Synthesis of fireworks-shaped ZnO/graphite-like carbon nanowires with enhanced visible-light photocatalytic activity and anti-photocorrosion, Colloids Surfaces A Physicochem. Eng. Asp. 518 (2017) 57–63. https://doi.org/10.1016/j.colsurfa.2016.12.050.

[36] N.P. de Moraes, L.A. Bacetto, C.M. Goes, G.V.J. Dantas, M.L.C.P. da Silva, L.A. Rodrigues, Desenvolvimento de compósitos ZnC_2O_4/xerogel de carbono para degradação fotocatalítica de azul de metileno sob radiação solar, Matéria (Rio Janeiro). 26 (2021). https://doi.org/10.1590/s1517-707620210002.12998.

[37] S. Alex Pandian, M. Sivakumar, Hoisting photovoltaic performance of perovskite $BaSnO_3$ nanoparticles wrapped reduced graphene oxide: Efficient photoelectrode for dye-sensitized solar cell, Mater. Today Proc. (2023) 1–7. https://doi.org/10.1016/j.matpr.2023.01.415.

[38] N.P. de Moraes, R.A. Pereira, T.V.C. da Silva, B.H.B. da Silva, G.P. de Assis, T.M.B. Campos, G.P. Thim, M.R. de Vasconcelos Lanza, L. de Freitas, L.A. Rodrigues, Cross-linked cellulose beads as an eco-friendly support for ZnO/SnO_2/carbon xerogel hybrid photocatalyst: Exploring the synergy between adsorption and photocatalysis under simulated sunlight, Int. J. Biol. Macromol. 254 (2024) 127826. https://doi.org/10.1016/j.ijbiomac.2023.127826.

[39] N.P. de Moraes, C.M. Goes, D.C. Sperandio, R. da S. Rocha, R. Landers, T. Paramasivam, L.A. Rodrigues, Development of a new zinc oxide/tin oxide/carbon xerogel photocatalyst for visible light photodegradation of 4-chlorophenol, Mater. Sci. Eng. B. 269 (2021) 115183. https://doi.org/10.1016/j.mseb.2021.115183.

[40] W. Shen, N. Zhu, J. Cui, H. Wang, Z. Dang, P. Wu, Y. Luo, C. Shi, Ecotoxicity monitoring and bioindicator screening of oil-contaminated soil during bioremediation, Ecotoxicol. Environ. Saf. 124 (2016) 120–128.

https://doi.org/10.1016/j.ecoenv.2015.10.005.

[41] T.A.G. Peduto, T.A. de Jesus, M.Y. Kohatsu, Sensibilidade de diferentes sementes em ensaio de fitotoxicidade, Rev. Bras. Ciência, Tecnol. e Inovação. 4 (2019) 200. https://doi.org/10.18554/rbcti.v4i2.3698.

[42] J. Charles, B. Sancey, N. Morin-Crini, P.-M. Badot, F. Degiorgi, G. Trunfio, G. Crini, Evaluation of the phytotoxicity of polycontaminated industrial effluents using the lettuce plant (Lactuca sativa) as a bioindicator, Ecotoxicol. Environ. Saf. 74 (2011) 2057–2064. https://doi.org/10.1016/j.ecoenv.2011.07.025.

[43] M.D. Gerber, T. Lucia, L. Correa, J.E.P. Neto, É.K. Correa, Phytotoxicity of effluents from swine slaughterhouses using lettuce and cucumber seeds as bioindicators, Sci. Total Environ. 592 (2017) 86–90. https://doi.org/10.1016/j.scitotenv.2017.03.075.

[44] G.L. de Arruda, G.K.A. de Moraes, A.F.C. Junior, A.R. Araujo, V.M. Chapla, Aromatic compounds from the endophytic fungus Asordaria conoidea and their allelochemical property using OSMAC strategy, Nat. Prod. Res. 36 (2022) 3999–4002. https://doi.org/10.1080/14786419.2021.1892098.

[45] N.P. de Moraes, R.D.M. dos Santos, M.E.V. Gouvêa, A. de Siervo, R. da Silva Rocha, D.A. Reddy, Y. Lianqing, M.R. de Vasconcelos Lanza, L.A. Rodrigues, Solar-based photocatalytic ozonation employing novel S-scheme ZnO/Cu_2O/CuO/carbon xerogel photocatalyst: effect of pH, salinity, turbidity, and temperature on salicylic acid degradation, Environ. Sci. Pollut. Res. 30 (2023) 98211–98230. https://doi.org/10.1007/s11356-023-29399-4.

[46] S. Pal, N. Sankar Das, B. Das, B. Kumar Das, S. Mukhopadhyay, K. Kumar Chattopadhyay, V doped $BaSnO_3$ nanocubes as a field emitting material: Experimental and theoretical investigation, Appl. Surf. Sci. 530 (2020) 147102. https://doi.org/10.1016/j.apsusc.2020.147102.

[47] A. Šarić, M. Vrankić, D. Lützenkirchen-Hecht, I. Despotović, Ž. Petrović, G. Dražić, F. Eckelt, Insight into the Growth Mechanism and Photocatalytic Behavior of Tubular Hierarchical ZnO Structures: An Integrated Experimental and Theoretical Approach, Inorg. Chem. 61 (2022) 2962–2979. https://doi.org/10.1021/acs.inorgchem.1c03905.

[48] J.G.M. de Sousa, T.V.C. da Silva, N.P. de Moraes, M.L. Caetano Pinto da Silva, R. da Silva Rocha, R. Landers, L.A. Rodrigues, Visible light-driven ZnO/g-C_3N_4/carbon xerogel ternary photocatalyst with enhanced activity for 4-chlorophenol degradation, Mater. Chem. Phys. 256 (2020) 123651. https://doi.org/10.1016/j.matchemphys.2020.123651.

[49] N.P. de Moraes, R. da Silva Rocha, M.L. Caetano Pinto da Silva, T.M. Bastos Campos, G.P. Thim, R. Landers, L.A. Rodrigues, Facile preparation of Bi-doped ZnO/β-Bi_2O_3/Carbon xerogel composites towards visible-light photocatalytic applications: Effect of calcination temperature and bismuth content, Ceram. Int. 46 (2020) 23895–23909. https://doi.org/10.1016/j.ceramint.2020.06.166.

[50] N.P. de Moraes, L.G.P. Marins, M.Y. de Moura Yamanaka, R. Bacani, R. da Silva Rocha, L.A. Rodrigues, Efficient photodegradation of 4-chlorophenol under solar radiation using a new ZnO/ZnS/carbon xerogel composite as a photocatalyst, J. Photochem. Photobiol. A Chem. 418 (2021) 113377. https://doi.org/10.1016/j.jphotochem.2021.113377.

[51] S. Vahabirad, A. Nezamzadeh-Ejhieh, Co-precipitation synthesis of BiOI/$(BiO)_2CO_3$: Brief characterization and the kinetic study in the photodegradation and mineralization of sulfasalazine, J. Solid State Chem. 310 (2022) 123018. https://doi.org/10.1016/j.jssc.2022.123018.

[52] T. Tamiji, A. Nezamzadeh-Ejhieh, Study of kinetics aspects of the electrocatalytic oxidation of benzyl alcohol in aqueous solution on AgBr modified carbon paste electrode, Mater. Chem. Phys. 237 (2019) 121813. https://doi.org/10.1016/j.matchemphys.2019.121813.

[53] G.V. Jucá Dantas, N.P. de Moraes, R. Bacani, L.Á. Rodrigues, Facile synthesis of cadmium sulfide and the effect of thermal annealing in N_2-rich atmosphere on its structural, morphological, chemical, and optical properties, Mater. Chem. Phys. 277 (2022) 125492. https://doi.org/10.1016/j.matchemphys.2021.125492.

[54] N.P. de Moraes, R.B. Valim, R. da Silva Rocha, M.L.C.P. da Silva, T.M.B. Campos, G.P. Thim, L.A. Rodrigues, Effect of synthesis medium on structural and photocatalytic properties of ZnO/carbon xerogel composites for solar and visible light degradation of 4-chlorophenol and bisphenol A, Colloids Surfaces A

Physicochem. Eng. Asp. 584 (2020) 124034. https://doi.org/10.1016/j.colsurfa.2019.124034.

[55] N.P. de Moraes, F.A. Torezin, G.V. Jucá Dantas, J.G.M. de Sousa, R.B. Valim, R. da Silva Rocha, R. Landers, M.L.C.P. da Silva, L.A. Rodrigues, TiO_2/Nb_2O_5/carbon xerogel ternary photocatalyst for efficient degradation of 4-chlorophenol under solar light irradiation, Ceram. Int. 46 (2020) 14505–14515. https://doi.org/10.1016/j.ceramint.2020.02.249.

[56] J. John, S. S, S. Pillai.S, R. Philip, V.P.M. Pillai, Effect of Fe doping on the structural, morphological, optical, magnetic and dielectric properties of $BaSnO_3$, J. Mater. Sci. Mater. Electron. 32 (2021) 11763–11780. https://doi.org/10.1007/s10854-021-05806-9.

[57] A. Marikutsa, M. Rumyantseva, A. Baranchikov, A. Gaskov, Nanocrystalline $BaSnO_3$ as an Alternative Gas Sensor Material: Surface Reactivity and High Sensitivity to SO_2, Materials (Basel). 8 (2015) 6437–6454. https://doi.org/10.3390/ma8095311.

[58] S. Moshtaghi, S. Zinatloo-Ajabshir, M. Salavati-Niasari, Preparation and characterization of $BaSnO_3$ nanostructures via a new simple surfactant-free route, J. Mater. Sci. Mater. Electron. 27 (2016) 425–435. https://doi.org/10.1007/s10854-015-3770-0.

[59] S. Sumithra, N.V. Jaya, Structural, optical and magnetization studies of Fe-doped $CaSnO_3$ nanoparticles via hydrothermal route, J. Mater. Sci. Mater. Electron. 29 (2018) 4048–4057. https://doi.org/10.1007/s10854-017-8348-6.

[60] N.P. de Moraes, L.H.A. Roupinha, G.S. dos Santos, B.R.C. de Menezes, J.G.M. de Sousa, G.V.J. Dantas, L. Chaguri, L.A. Rodrigues, Synthesis, characterization and application of Nb_2O_5-doped zinc oxide for solar-based photodegradation of 4-chlorophenol, Mater. Lett. 275 (2020) 128156. https://doi.org/10.1016/j.matlet.2020.128156.

[61] N.P. de Moraes, R. da Silva Rocha, A. de Siervo, C.C.A. do Prado, T.C.B. de Paiva, T.M.B. Campos, G.P. Thim, M.R. de Vasconcelos Lanza, L.A. Rodrigues, Resorcinol-based carbon xerogel/ZnO composite for solar-light-induced photodegradation of sulfamerazine, Opt. Mater. (Amst). 128 (2022) 112470.

https://doi.org/10.1016/j.optmat.2022.112470.

[62] K.K. James, A. Aravind, M.K. Jayaraj, Structural, optical and magnetic properties of Fe-doped barium stannate thin films grown by PLD, Appl. Surf. Sci. 282 (2013) 121–125. https://doi.org/10.1016/j.apsusc.2013.05.076.

[63] A. Roy, P.P. Das, P. Selvaraj, S. Sundaram, P.S. Devi, Perforated $BaSnO_3$ Nanorods Exhibiting Enhanced Efficiency in Dye Sensitized Solar Cells, ACS Sustain. Chem. Eng. 6 (2018) 3299–3310. https://doi.org/10.1021/acssuschemeng.7b03479.

[64] N.P. de Moraes, M.B. de C. Sanmartin, R. da Silva Rocha, A. de Siervo, M.R. de Vasconcelos Lanza, D.A. Reddy, L. Yu, L.A. Rodrigues, ZnO/CeO_2/carbon xerogel composites with direct Z-scheme heterojunctions: Enhancing photocatalytic remediation of 4-chlorophenol under visible light, J. Rare Earths. (2022). https://doi.org/10.1016/j.jre.2022.11.001.

[65] R. Cuscó, E. Alarcón-Lladó, J. Ibáñez, L. Artús, J. Jiménez, B. Wang, M.J. Callahan, Temperature dependence of Raman scattering in ZnO, Phys. Rev. B. 75 (2007) 165202. https://doi.org/10.1103/PhysRevB.75.165202.

[66] A.S. Deepa, S. Vidya, P.C. Manu, S. Solomon, A. John, J.K. Thomas, Structural and optical characterization of $BaSnO_3$ nanopowder synthesized through a novel combustion technique, J. Alloys Compd. 509 (2011) 1830–1835. https://doi.org/10.1016/j.jallcom.2010.10.056.

[67] M. Asisi Janifer, S. Anand, C. Joseph Prabagar, S. Pauline, Structural and optical properties of $BaSnO_3$ ceramics by solid state reaction method, Mater. Today Proc. 47 (2021) 2067–2070. https://doi.org/10.1016/j.matpr.2021.04.429.

[68] N. Ghobadi, Band gap determination using absorption spectrum fitting procedure, Int. Nano Lett. 3 (2013) 2. https://doi.org/10.1186/2228-5326-3-2.

[69] M. Farsi, A. Nezamzadeh-Ejhieh, A Z-scheme Cobalt(II) oxide-silver tungstate nano photocatalyst: Experimental design and mechanism study for the degradation of methylene blue, Surfaces and Interfaces. 32 (2022) 102148. https://doi.org/10.1016/j.surfin.2022.102148.

[70] S.A. Mirsalari, A. Nezamzadeh-Ejhieh, Focus on the photocatalytic pathway of

the CdS-AgBr nano-catalyst by using the scavenging agents, Sep. Purif. Technol. 250 (2020) 117235. https://doi.org/10.1016/j.seppur.2020.117235.

[71] N. Mehrabanpour, A. Nezamzadeh-Ejhieh, S. Ghattavi, A. Ershadi, A magnetically separable clinoptilolite supported CdS-PbS photocatalyst: Characterization and photocatalytic activity toward cefotaxime, Appl. Surf. Sci. 614 (2023) 156252. https://doi.org/10.1016/j.apsusc.2022.156252.

[72] N.P. de Moraes, G.S. dos Santos, G.C. Neves, R.B. Valim, R. da Silva Rocha, R. Landers, M.L. Caetano Pinto da Silva, L.A. Rodrigues, Development of Nb_2O_5-doped ZnO/Carbon xerogel photocatalyst for the photodegradation of 4-chlorophenol, Optik (Stuttg). 219 (2020) 165238. https://doi.org/10.1016/j.ijleo.2020.165238.

[73] N.P. de Moraes, M.L.C.P. da Silva, T.M.B. Campos, G.P. Thim, L.A. Rodrigues, Novel synthetic route for low-cost carbon-modified TiO_2 with enhanced visible light photocatalytic activity: carbon content and calcination effects, J. Sol-Gel Sci. Technol. 87 (2018) 380–390. https://doi.org/10.1007/s10971-018-4700-4.

[74] P. Rajasekaran, M. Arivanandhan, N. Sato, Y. Kumaki, T. Mori, Y. Hayakawa, K. Hayakawa, Y. Kubota, R. Jayavel, M. Shimomura, The effect of Sr and Sb co-doping on structural, morphological and thermoelectric properties of $BaSnO_3$ perovskite material, J. Alloys Compd. 894 (2022) 162335. https://doi.org/10.1016/j.jallcom.2021.162335.

[75] J. Ângelo, P. Magalhães, L. Andrade, A. Mendes, Characterization of TiO_2-based semiconductors for photocatalysis by electrochemical impedance spectroscopy, Appl. Surf. Sci. 387 (2016) 183–189. https://doi.org/10.1016/j.apsusc.2016.06.101.

[76] P.J.M. Cordeiro Junior, R.S. Souto, M. de O. Almeida, G.B.S. Pereira, M.A. Franco, K.M. Honorio, F.V. Rocha, M.R. de V. Lanza, A combined approach toward enhancing 2-electron oxygen reduction through the incorporation of Pd-based complex into a carbonaceous matrix: Experimental and mechanistic-theoretical studies, Electrochim. Acta. 460 (2023) 142543. https://doi.org/10.1016/j.electacta.2023.142543.

[77] A. Barranco-López, A.I. Moral-Rodríguez, E. Fajardo-Puerto, A. Elmouwahidi,

E. Bailón-García, Highly graphitic Fe-doped carbon xerogels as dual-functional electro-Fenton catalysts for the degradation of tetracycline in wastewater, Environ. Res. 228 (2023) 115757. https://doi.org/10.1016/j.envres.2023.115757.

[78] J. Cai, S. Hu, J. Xiang, H. Zhang, D. Men, The effect of graphitized carbon on the adsorption and photocatalytic degradation of methylene blue over TiO_2/C composites, RSC Adv. 10 (2020) 40830–40842. https://doi.org/10.1039/D0RA01105C.

[79] J. Xu, P. Liang, X. Shen, F. Wang, Y. Lou, J. Zhang, C. Pan, Y. Zhu, Z. Wang, High-efficiency removal of organic pollutants, antibiotic resistant bacteria and resistance genes by a photocatalysis-self-Fenton system based on S, K co-doped g-C_3N_4 nanosheets, Sep. Purif. Technol. 339 (2024) 126734. https://doi.org/10.1016/j.seppur.2024.126734.

[80] R. Fagan, D.E. McCormack, D.D. Dionysiou, S.C. Pillai, A review of solar and visible light active TiO_2 photocatalysis for treating bacteria, cyanotoxins and contaminants of emerging concern, Mater. Sci. Semicond. Process. 42 (2016) 2–14. https://doi.org/10.1016/j.mssp.2015.07.052.

[81] Y. Nosaka, A.Y. Nosaka, Generation and Detection of Reactive Oxygen Species in Photocatalysis, Chem. Rev. 117 (2017) 11302–11336. https://doi.org/10.1021/acs.chemrev.7b00161.

[82] J. Zhang, Y. Nosaka, Mechanism of the OH Radical Generation in Photocatalysis with TiO_2 of Different Crystalline Types, J. Phys. Chem. C. 118 (2014) 10824–10832. https://doi.org/10.1021/jp501214m.

[83] J. qi Li, Z. wei Zhou, X. Li, Y. ling Yang, J. feng Gao, R. Yu, H. ping Wang, N. Wang, Synergistically boosting sulfamerazine degradation via activation of peroxydisulfate by photocatalysis of Bi_2O_3-TiO_2/PAC under visible light irradiation, Chem. Eng. J. 428 (2022). https://doi.org/10.1016/j.cej.2021.132613.

[84] S. Yi, X. Yue, D. Xu, Z. Liu, F. Zhao, D. Wang, Y. Lin, Study on photogenerated charge transfer properties and enhanced visible-light photocatalytic activity of p-type Bi_2O_3 /n-type ZnO heterojunctions, New J. Chem. 39 (2015) 2917–2924. https://doi.org/10.1039/C4NJ01738B.

[85] B. Pourrut, M. Shahid, C. Dumat, P. Winterton, E. Pinelli, Lead Uptake,

Toxicity, and Detoxification in Plants, in: 2011: pp. 113–136. https://doi.org/10.1007/978-1-4419-9860-6_4.

[86] C. Vieira, C. Marcon, A. Droste, Phytotoxic and cytogenotoxic assessment of glyphosate on Lactuca sativa L., Brazilian J. Biol. 84 (2024). https://doi.org/10.1590/1519-6984.257039.

[87] S. Ahmed, M.G. Rasul, W.N. Martens, R. Brown, M.A. Hashib, Advances in Heterogeneous Photocatalytic Degradation of Phenols and Dyes in Wastewater: A Review, Water, Air, Soil Pollut. 215 (2011) 3–29. https://doi.org/10.1007/s11270-010-0456-3.

[88] N.P. de Moraes, A. de Siervo, T.O. Silva, R. da Silva Rocha, D.A. Reddy, Y. Lianqing, M.R. de Vasconcelos Lanza, L.A. Rodrigues, Kraft lignin-based carbon xerogel/zinc oxide composite for 4-chlorophenol solar-light photocatalytic degradation: effect of pH, salinity, and simultaneous Cr(VI) reduction, Environ. Sci. Pollut. Res. 30 (2023) 8280–8296. https://doi.org/10.1007/s11356-022-22825-z.

[89] C.-C. Yang, C.-L. Huang, T.-C. Cheng, H.-T. Lai, Inhibitory effect of salinity on the photocatalytic degradation of three sulfonamide antibiotics, Int. Biodeterior. Biodegradation. 102 (2015) 116–125. https://doi.org/10.1016/j.ibiod.2015.01.015.

[90] A.T. Le, N.S.B. Samsuddin, S.-L. Chiam, S.-Y. Pung, Synergistic effect of pH solution and photocorrosion of ZnO particles on the photocatalytic degradation of Rhodamine B, Bull. Mater. Sci. 44 (2021) 5. https://doi.org/10.1007/s12034-020-02281-6.

[91] D. Zhang, S. Lv, Z. Luo, A study on the photocatalytic degradation performance of a $[KNbO_3]_{0.9}$-$[BaN_{0.5}Nb_{0.5}O_{3-\delta}]_{0.1}$ perovskite, RSC Adv. 10 (2020) 1275–1280. https://doi.org/10.1039/C9RA07310H.

[92] A. Kumar, A Review on the Factors Affecting the Photocatalytic Degradation of Hazardous Materials, Mater. Sci. Eng. Int. J. 1 (2017). https://doi.org/10.15406/mseij.2017.01.00018.

Declaration of interests

☒ The authors declare that they have no known competing financial interests or personal relationships that could have appeared to influence the work reported in this paper.

☐The authors declare the following financial interests/personal relationships which may be considered as potential competing interests: